ACS APPLIED MATERIALS & INTERFACES

www.acsami.org

Research Article

Realization of Ethylene Production from Its Quaternary Mixture through Metal−Organic Framework Materials

Xin Zhang, Hui Cui, Rui-Biao Lin,* Rajamani Krishna, Zhi-Yin Zhang, Ting Liu, Bin Liang, and Banglin Chen*

Cite This: *ACS Appl. Mater. Interfaces* 2021, 13, 22514−22520

Read Online

ACCESS | Metrics & More | Article Recommendations | Supporting Information

ABSTRACT: Ethylene production from oxidative coupling of methane is a sustainable and economically attractive alternative to that through traditional hydrocarbon cracking technology. However, efficient ethylene separation from the complex reaction mixture is a daunting challenge that hinders the practical adoption of this technology. Herein, we report the efficient adsorptive separation of the $CH_4/CO_2/C_2H_4/C_2H_6$ mixture using three representative metal−organic frameworks (MOFs) (UTSA-74, MOF-74, and HKUST-1) with diverse open metal sites. The efficient separation relies on tuning the selectivity through the convergence of characteristics including Lewis acidity of open metal sites, pore space, and cooperative binding behavior. The separation performance of these materials has been evaluated through single-component gas adsorption and dynamic breakthrough experiments. HKUST-1 provides the highest separation potential (4.1 mmol/g) thanks to its simultaneously high ideal adsorbed solution theory (IAST) selectivity and ethylene adsorption capacity, representing a benchmark material for such a challenging quaternary separation.

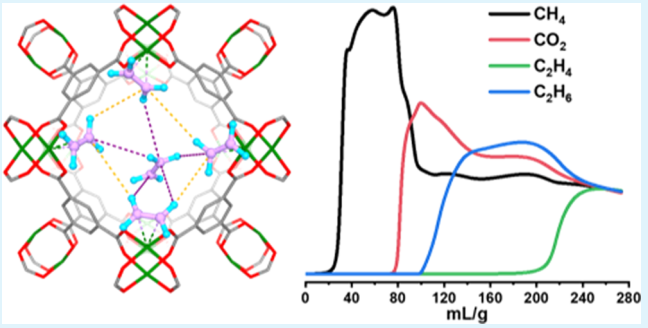

KEYWORDS: *metal−organic frameworks, ethylene, separation, oxidative coupling of methane, open metal site*

INTRODUCTION

Due to the increase of global climate change and environmental concerns, researchers have been seeking alternative supplies of chemical feedstocks to reduce dependence on fossil fuels. Ethylene (C_2H_4) is the largest petrochemical feedstock to produce widely used polypropylene and other chemical commodities. The annual production of ethylene was more than 170 million tons globally in 2016, mainly by cracking of naphtha or ethane (C_2H_6).[1] There have been many attempts to produce ethylene through conversions of single-carbon species such as methane and carbon dioxide. One alternative ethylene production method, oxidative coupling of methane (OCM),[2−4] has attracted great attention during the past several decades. Methane (CH_4) is mainly used as fuel for power and heat generation, owing to its high abundance and low cost. Upgrading methane to higher hydrocarbons such as valuable ethylene is of great economic and environmental benefits. Besides, methane can be generated from renewable sources such as biogas[5] and catalytic CO_2 reduction,[6] which enables sustainable ethylene production from the OCM process.

In a typical OCM process, the product contains certain amounts of unreacted CH_4 and byproducts including C_2H_6 and CO_2 together with C_2H_4.[7] The low yield of C_2H_4 and complex product composition make the separation of C_2H_4 very difficult by conventional distillation. A feasible solution is using porous adsorbents to selectively extract C_2H_4 from the mixture, while the unreacted CH_4 can be recycled for a new reaction cycle.[7,8]

As emerging porous materials, metal−organic frameworks (MOFs) have demonstrated advanced performance in a variety of applications such as catalysis,[9−11] water harvest,[12,13] biomedicine,[14,15] gas storage,[16−20] and separation.[21−25] Tremendous progress has been made for the separation of binary gas mixtures through finely tuning the pore aperture size,[26−31] surface functionality,[1,32−36] and flexibility.[37−41] Separations of the ternary or quaternary mixtures are less explored and much more challenging.[42−44] For the OCM reaction mixture ($CH_4/CO_2/C_2H_4/C_2H_6$), CH_4 generally has weak interaction with adsorbents and low adsorption capacity. Some MOF materials like HKUST-1 have shown selective adsorption of CO_2 and C2 hydrocarbons over CH_4 in corresponding mixtures.[45,46] The grand challenge is simulta-

Received: March 1, 2021
Accepted: April 28, 2021
Published: May 6, 2021

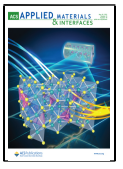

https://doi.org/10.1021/acsami.1c03923
ACS Appl. Mater. Interfaces 2021, 13, 22514−22520

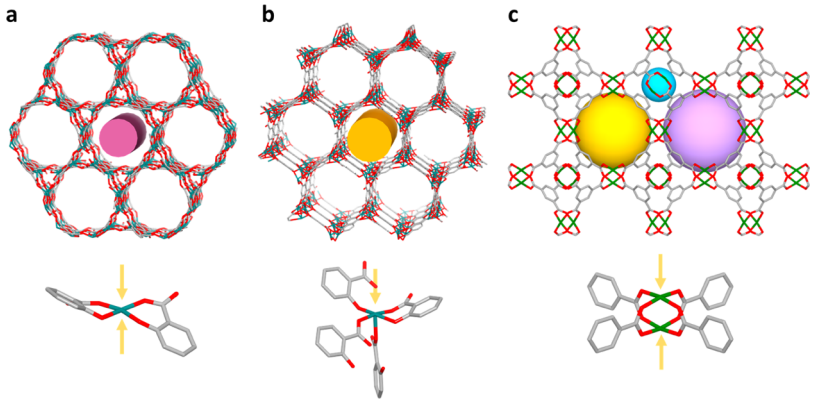

Figure 1. Crystal structure, pore geometry, and open metal sites of MOFs studied. (a) UTSA-74; (b) MOF-74; and (c) HKUST-1. Yellow arrows indicate the guest accessible sites of metals in each framework.

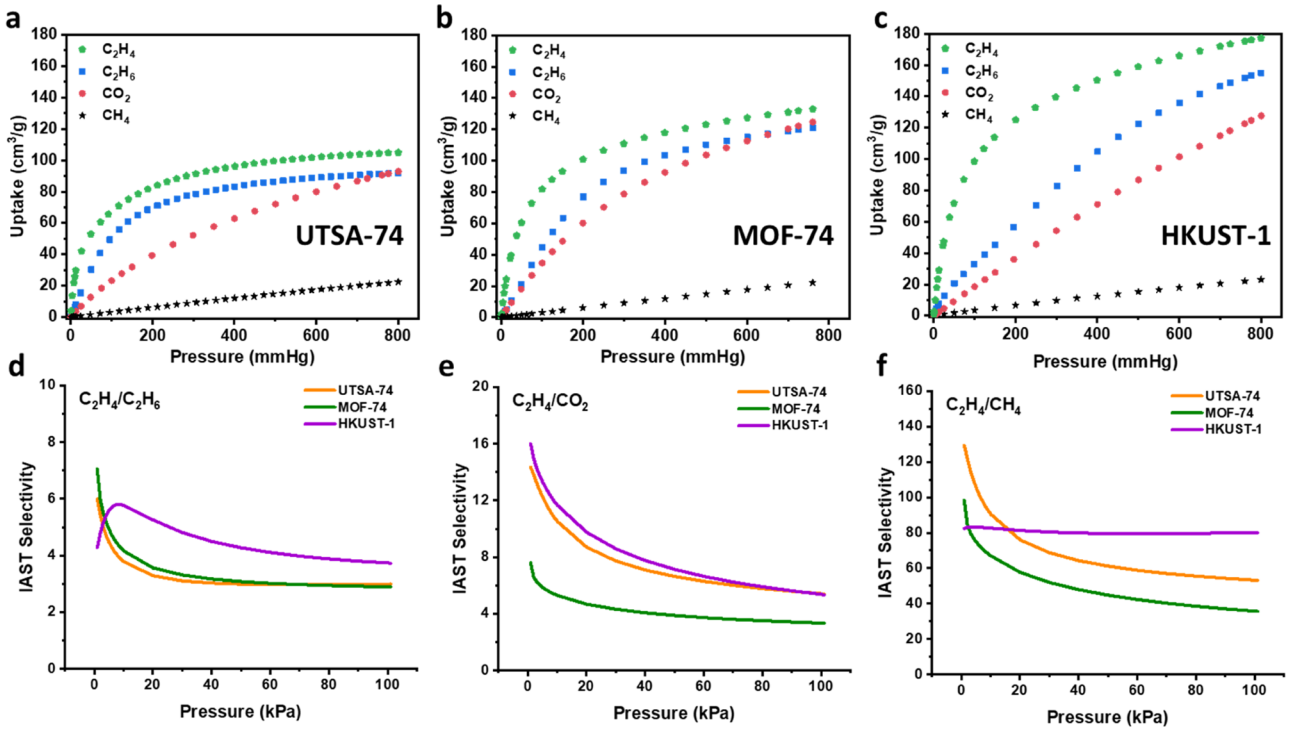

Figure 2. Gas adsorption isotherms and IAST selectivity. CH_4, CO_2, C_2H_4, and C_2H_6 adsorption isotherms at 298 K of UTSA-74 (a), MOF-74 (b), and HKUST-1 (c). IAST selectivity of MOFs studied: (d) C_2H_4/C_2H_6, (e) C_2H_4/CO_2, and (f) C_2H_4/CH_4.

neous C_2H_4/C_2H_6 and C_2H_4/CO_2 separation, and multiple adsorbents were adopted sometimes.[42] The kinetic diameter of C_2H_4 (4.163 Å) falls between those of CO_2 (3.300 Å) and C_2H_6 (4.443 Å),[47] which makes sieving separation extremely difficult. The preferential binding of C_2H_4 over C_2H_6 at open metal sites (OMS) of MOFs through pi complexation is an efficient strategy for C_2H_4/C_2H_6 separation.[32] However, such a strategy becomes quite complicated in the presence of CO_2, which has a higher quadrupole moment[47] (1.5×10^{-26} esucm^2 for C_2H_4 and 4.3×10^{-26} esucm^2 for CO_2) and coordinates to open metal sites through Lewis acid−base interaction.[48] Our previous discovery of UTSA-74 revealed that the orientation of open metal sites could affect the binding mode and adsorption capacity of CO_2.[49] At the same time, in consideration of the different binding mechanisms of C_2H_4 and CO_2, weaker Lewis acid might preferentially adsorb C_2H_4 over CO_2 due to its weaker binding affinity toward CO_2.[48,50,51] Therefore, we envision that pore structure engineering of MOF materials could realize the challenging C_2H_4/CO_2 separation and eventually lead to efficient $CH_4/CO_2/C_2H_4/C_2H_6$ separation.

Herein, we report selective adsorption of C_2H_4 from the $CH_4/CO_2/C_2H_4/C_2H_6$ (1/1/1/1, v/v/v/v) mixture by three MOF materials (MOF-74, UTSA-74, and HKUST-1) with open metal sites and a diverse pore matrix. Gas adsorption isotherms and dynamic breakthrough studies demonstrated the successful separation with all three materials. Especially, HKUST-1 with the highest selectivity and C_2H_4 adsorption capacity exhibits large separation potential, representing a benchmark material for such separation. These encouraging results highlight the great potential of MOFs with open metal sites and tunable pore structures for multicomponent separation and bring promise for alternative ethylene production by oxidative coupling of methane.

https://doi.org/10.1021/acsami.1c03923
ACS Appl. Mater. Interfaces 2021, 13, 22514−22520

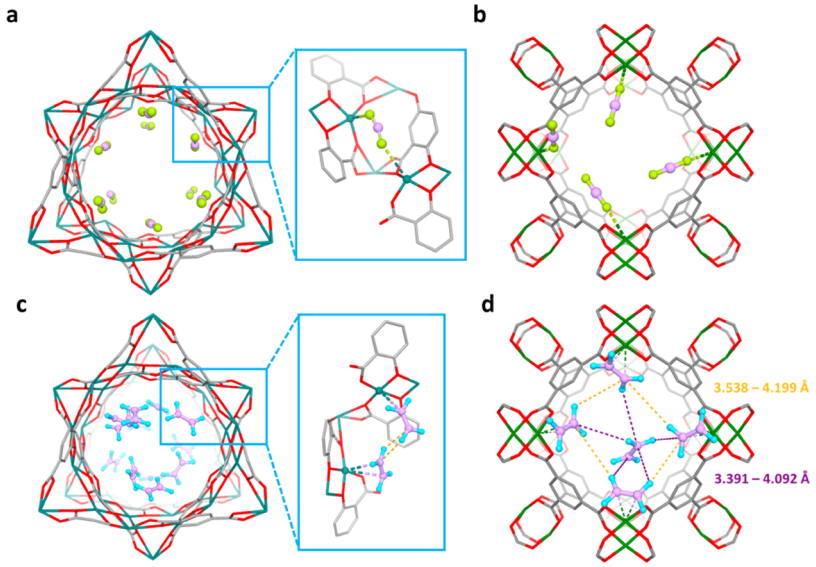

Figure 3. Cooperative host–guest and guest–guest interactions. (a) Bridged CO_2 binding at open metal sites of UTSA-74 as revealed by single-crystal X-ray diffraction.[49] (b) CO_2 binding at open metal sites of HKUST-1. (c) Ethylene binding at open metal sites of UTSA-74 (d) Ethylene binding at open metal sites and supramolecular assembly in HKUST-1. (b–d) Optimized structures with loaded guests by the GCMC simulations.

RESULTS AND DISCUSSION

Three representative MOF materials (UTSA-74,[49] MOF-74,[52] and HKUST-1[53,54]) with weak Lewis acidic sites and diverse pore structures were chosen to evaluate the $CH_4/CO_2/C_2H_4/C_2H_6$ separation performance. The Zn of MOF-74 is in the square-pyramidal coordination mode with one open site, while Zn in its isomeric structure UTSA-74 features two accessible binding sites in the square planner coordination geometry (Figure 1a,b). The Cu of HKUST-1 in the square planar coordination geometry forms a paddle-wheel unit with one open site per metal (Figure 1c). UTSA-74 and MOF-74 feature a one-dimensional (1D) open channel, while HKUST-1 possesses three types of cages (Figure 1a–c). These three materials were synthesized by solvothermal reactions and their phase purity was confirmed by powder X-ray diffraction (PXRD) measurements (Figures S1–S3), which matches well with simulated patterns from single-crystal structures.

Upon activation, the permanent porosity of these materials was established by N_2 adsorption at 77 K (Figures S4–S6). According to the adsorption isotherms, the Brunauer–Emmett–Teller (BET) surface areas were calculated to be 711 m^2/g for UTSA-74, 915 m^2/g for MOF-74, and 1589 m^2/g for HKUST-1. Further, the pore volumes were determined to be 0.37 cm^3/g for UTSA-74, 0.47 cm^3/g for MOF-74, and 0.77 cm^3/g for HKUST-1, which match well with their theoretical pore volumes calculated by PLATON based on their crystal structures (Table S1).

The separation performance was first studied by single-component gas adsorption isotherms at 298 K. As expected, these materials with weak Lewis acidic sites exhibit selective adsorption of C_2H_4 over the coordinatively competitive CO_2 molecule, as well as the saturated hydrocarbons CH_4 and C_2H_6. The C_2H_4 adsorption capacity of HKUST-1 reached 175 cm^3/g at 1 bar being the highest among all three materials, followed by those of MOF-74 (133 cm^3/g) and UTSA-74 (104 cm^3/g). The C_2H_4 packing densities were further calculated to be 12.4 $mmol/cm^3$ for UTSA-74, 12.6 $mmol/cm^3$ for MOF-74, and 10.1 $mmol/cm^3$ for HKUST-1. With the highest pore volume, HKUST-1 yields the highest C_2H_4 adsorption capacity and slightly lower packing density.

Next, we applied the well-established ideal adsorbed solution theory (IAST)[55] to evaluate the C_2H_4/C_2H_6, C_2H_4/CO_2, and C_2H_4/CH_4 selectivities of these materials (see fitting parameters in Tables S2–S4). For C_2H_4/C_2H_6, the IAST selectivity of HKUST-1 (3.7) is higher than those of UTSA-74 (3.0) and MOF-74 (2.9), as shown in Figure 2d. HKUST-1 and UTSA-74 exhibit the same C_2H_4/CO_2 selectivity (5.4), which is higher than that of MOF-74 (3.3). For C_2H_4/CH_4, all three materials exhibit quite high selectivities (80.2 for HKUST-1, 53.2 for UTSA-74, and 35.7 for MOF-74), which can be attributed to the much weaker host–guest interaction and lower uptake of CH_4. Overall, HKUST-1 has the highest selectivity among these three materials for C_2H_4/C_2H_6, C_2H_4/CO_2, and C_2H_4/CH_4 binary mixtures.

The high C_2H_4/CO_2 selectivity of UTSA-74 is because half of the open metal sites are hindered by the CO_2 molecule coordinated on the neighbor Zn open site. As revealed by single-crystal X-ray diffraction[49] (Figure 3a), the two oxygen atoms of the CO_2 molecule coordinate with two Zn atoms in the bridged form with bond lengths of 2.177 and 3.170 Å. Such a unique coordination mode could only be formed with the proper distance and direction of the open metal sites. In comparison, C_2H_4 binds the open metal sites with one molecule in regular coordination with the pi bond, and the neighboring molecule coordinates with one sp^2 carbon in the predicted C_2H_4 binding structure by the grand canonical Monte Carlo (GCMC) simulations. Hydrogen bonding interactions between neighboring C_2H_4 molecules were also found (Figure 3c).

To understand the superior selectivity of HKUST-1, we further studied the interaction between C_2H_4 and the HKUST-1 framework. GCMC calculations revealed that C_2H_4 molecules are primarily binding to open metal sites with bond lengths in the range of 2.4–2.8 Å, as shown in Figure 3d. These coordinated C_2H_4 molecules also formed multiple weak hydrogen bonding (H···C) interactions with each other as well as uncoordinated C_2H_4 molecules. The intermolecular C–

https://doi.org/10.1021/acsami.1c03923
ACS Appl. Mater. Interfaces 2021, 13, 22514–22520

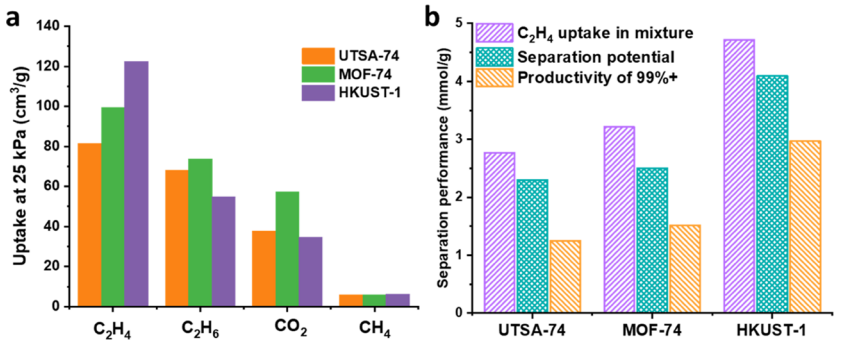

Figure 4. Adsorption and separation properties of UTSA-74, MOF-74, and HKUST-1. (a) Adsorption capacity of C_2H_4, C_2H_6, and CO_2 at 25 kPa. (b) Theoretical values of separation potential, productivity of 99%+, and C_2H_4 uptake in the mixture of $CH_4/CO_2/C_2H_4/C_2H_6$ (1/1/1/1, v/v/v/v) at 1 bar.

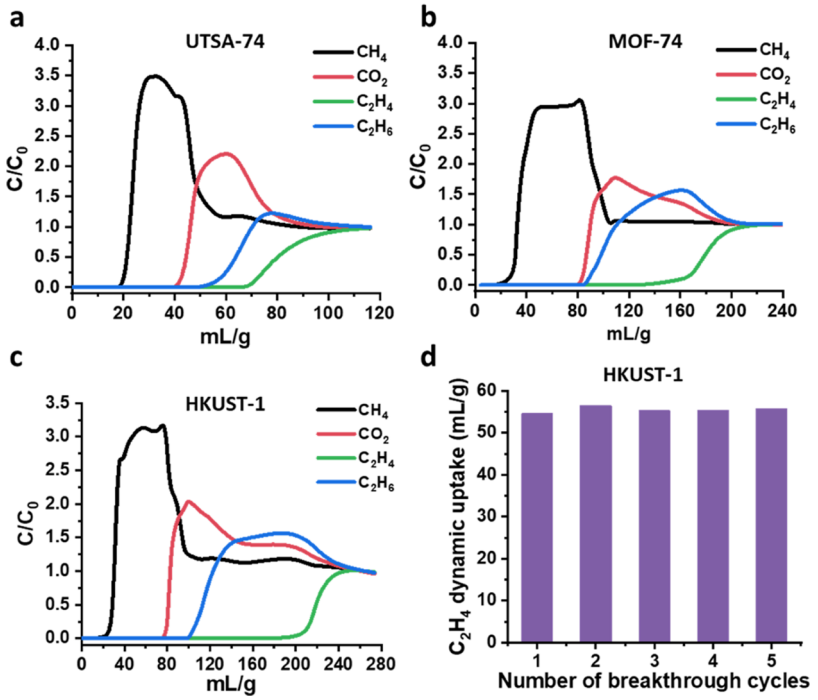

Figure 5. Breakthrough separation of $CH_4/CO_2/C_2H_4/C_2H_6$ (1/1/1/1, v/v/v/v) under 298 K and 1 bar with UTSA-74 (a), MOF-74 (b), and HKUST-1 (c). (d) Dynamic C_2H_4 uptake of HKUST-1 during five repeated breakthrough cycles.

H···$\pi_{(ethylene)}$ distances between ethylene molecules are in the range of 3.391−4.199 Å being comparable to those in NOTT-300 (3.82−4.62 Å).[35] The appropriate pore space in HKUST-1 and the open metal sites collaboratively made it show high C_2H_4 adsorption, whereas relatively low C_2H_6 adsorption, especially at low pressure (25 kPa, Figure 4a), thus showing the highest C_2H_4/C_2H_6 selectivity among these adsorbents. The ratio of adsorbed C_2H_4 to OMS is 3.1, which is much higher than those of UTSA-74 (0.74) and MOF-74 (0.95), indicating these two MOFs adsorb C_2H_4 primarily at open metal sites (Figure S7). In comparison, no obvious guest−guest interaction was found in the CO_2-loaded structure, only CO_2 coordination at open metal sites and van der Waals interaction with the frameworks were observed (Figure 3b).

For the separation of the $CH_4/CO_2/C_2H_4/C_2H_6$ (1/1/1/1, v/v/v/v) mixture at 101 kPa, the partial pressure of each component is ∼25 kPa. Compared with UTSA-74 and MOF-74, HKUST-1 adsorbed the highest amount of C_2H_4, while the lowest amount of CO_2 and C_2H_6 at 25 kPa, as shown in Figure 4a. The CO_2 adsorption of HKUST-1 is slightly lower than that of UTSA-74 and much lower than that of MOF-74. The stronger guest−guest interaction together with π complexation of C_2H_4 in HKUST-1 facilitated high adsorption capacity at a low-pressure region. The heat of adsorption was also calculated based on adsorption isotherms at 298 and 273 K using the Virial method (Figures S8−S13). Since the C_2H_4 adsorption of HKUST-1 is promoted by weak hydrogen bonding interactions, its Q_{st} is ∼26 kJ/mol, which is comparable to that of MOF-74 and smaller than that of UTSA-74. The low Q_{st} of HKUST-1 is preferred for the easy regeneration of the material with low energy penalty.

Considering contributions from both selectivity and adsorption capacity, we further calculated the separation potential[56] to evaluate the separation performance of the $CH_4/CO_2/C_2H_4/C_2H_6$ mixture. As shown in Figure 4b and Table S5, HKUST-1 exhibits much higher separation potential (4.1 mmol/g) than those of UTSA-74 (2.3 mmol/g) and MOF-74 (2.5 mmol/g), representing a new benchmark for

https://doi.org/10.1021/acsami.1c03923
ACS Appl. Mater. Interfaces 2021, 13, 22514−22520

$CH_4/CO_2/C_2H_4/C_2H_6$ separation. The C_2H_4 uptakes from the quaternary mixture were calculated to be 2.77 mmol/g for UTSA-74, 3.22 mmol/g for MOF-74, and 4.72 mmol/g for HKUST-1. Such superiority of HKUST-1 can be attributed to its simultaneously high selectivity and high adsorption capacity as discussed above.

With these encouraging results, we carried out transient breakthrough simulations to evaluate the separation performance under dynamic conditions. As expected, all three MOFs can separate C_2H_4 from the $CH_4/CO_2/C_2H_4/C_2H_6$ (1/1/1/1, v/v/v/v) mixture (Figures S15a, S16a, and S17a). Interestingly, CO_2 eluted out before C_2H_6 for UTSA-74 and HKUST-1, while these two gases break through almost simultaneously for MOF-74. The breakthrough order of UTSA-74 and HKUST-1 is quite unique because MOFs with open metal sites usually bind CO_2 stronger than C_2H_6, which leads to the opposite $CO_2-C_2H_6$ breakthrough order.[8] The unique property of UTSA-74 and HKUST-1 enables the simultaneous capture of valuable C2 hydrocarbons, providing extra benefit besides C_2H_4 recovery alone. The productivity of the 99%+ pure C_2H_4 product was determined by transient desorption simulations (Figures S15b, S16b, and S17b). Following the same trend of separation potential, HKUST-1 yields the highest productivity of 2.97 mmol/g (Figure 4b and Table S5).

Breakthrough experiments of these materials have been conducted with the modeling $CH_4/CO_2/C_2H_4/C_2H_6$ (1/1/1/1, v/v/v/v) gas mixture at 1 bar and 298 K under a flow rate of 2.0 mL/min. As shown in Figure 5a–c, the breakthrough order follows the simulated patterns quite well. The breakthrough volumes (converted from the flow rate and breakthrough time) of C_2H_4 are 76 mL/g for UTSA-74, 162 mL/g for MOF-74, and 219 mL/g for HKUST-1. The highest breakthrough volume for HKUST-1 can be attributed to its highest C_2H_4 adsorption capacity and separation potential. The dynamic uptakes were calculated to be 19 mL/g for UTSA-74, 41 mL/g for MOF-74, and 55 mL/g for HKUST-1. The HKUST-1 material can be facilely regenerated by purging with helium gas for 30 min under a flow rate of 50 mL/min at room temperature. A cyclic breakthrough experiment (Figures 5d and S19) demonstrated that HKUST-1 can be utilized for at least five cycles without an obvious change in their dynamic uptakes, indicating the satisfactory stability under testing conditions. Considering MOFs with OMSs are usually water-sensitive, for a humid OCM mixture in practical application, a predying process or further hydrophobic modification on MOF adsorbents is a feasible option.

CONCLUSIONS

In summary, we have evaluated three MOF materials with weak Lewis acidic open metal sites and diverse pore structures for C_2H_4 recovery from a quaternary OCM mixture. HKUST-1 with high C_2H_4 adsorption capacity and selectivity over C_2H_6, CO_2, and CH_4 provides the highest separation potential, representing a new benchmark material for such separation. Besides, UTSA-74 and HKUST-1 with high C_2H_4/CO_2 selectivity were able to simultaneously capture all valuable C2 hydrocarbons (C_2H_4 and C_2H_6). Investigation on the host–guest interaction revealed that the pore matrix (distance and orientation between open metal sites) played an important role in tuning the guest binding mode and adsorption capacity. Overall, this work brings great promise for alternative ethylene production from oxidative coupling of methane by efficient ethylene recovery from the reaction product mixture. The separation strategies of this work are expected to inspire and flourish the separation of multicomponent mixtures through tuning the pore matrix of MOFs with open metal sites.

EXPERIMENTAL SECTION

Materials, Instrument, and Simulation Details. All commercial chemicals were used without further purification unless otherwise mentioned. Compressed single-component gases (C_2H_6, C_2H_4, CH_4, CO_2, and N_2) and a mixture of $CH_4/CO_2/C_2H_4/C_2H_6$ (1/1/1/1, v/v/v/v) were all purchased from Airgas.

Powder X-ray diffraction (PXRD) data were collected on a Rigaku Smartlab3 X-ray powder diffractometer equipped with a Cu sealed tube (λ = 1.54178 Å) at room temperature. Gas sorption isotherms were measured using a Micromeritics ASAP 2020 system at various temperatures. The experimental temperatures were controlled by liquid nitrogen bath (77 K), ice-water bath (273 K), and water bath (298 K).

The breakthrough experiments were carried out in a self-made dynamic mixed-gas breakthrough setup. A stainless-steel column with inner dimensions of ϕ = 4 mm × 80 mm was used for sample packing. The mixed-gas flow and pressure were controlled by using a pressure-control valve and a mass flow controller. Outlet effluent from the column was continuously monitored using gas chromatography (GC-2014, Shimadzu) with a thermal conductivity detector (TCD). The column packed with the sample was first purged with a flow of He (70 mL/min) for 2 h at room temperature. The mixed-gas flow rate during the breakthrough process was 2 mL/min using the $CH_4/CO_2/C_2H_4/C_2H_6$ (1/1/1/1, v/v/v/v) mixture at room temperature (298 K).

The grand canonical Monte Carlo (GCMC) simulations were performed for CO_2 and C_2H_4 adsorption on HKUST-1, and C_2H_4 adsorption on UTSA-74. The MOF skeletons and gas molecules were both treated as rigid bodies. The saturation/maximum uptakes were modeled at 298 K using the fixed pressure task and the Metropolis method. The equilibration steps and the production steps were set to 1.0×10^5 and 1.0×10^6, respectively. The gas–framework interaction and the gas–gas interaction were described by the standard universal force field (UFF).

MOF Synthesis and Activation. Three MOF materials (UTSA-74,[49] MOF-74,[52] and HKUST-1[53,54]) were synthesized according to the literature methods. The as-synthesized materials were washed with fresh DMF 10 times during 24 h and fresh anhydrous methanol for 10 during another 24 h before transferring to the sample tube for activation on an ASAP 2020 machine. UTSA-74 was activated at 250 °C for 11 h until the pressure dropped to 7 μmHg, MOF-74 was activated at 180 °C for 11 h, and HKUST-1 was activated at 120 °C for 12 h.

ASSOCIATED CONTENT

Supporting Information

The Supporting Information is available free of charge at https://pubs.acs.org/doi/10.1021/acsami.1c03923.

PXRD; adsorption isotherm; calculation of IAST selectivity; Q_{st}; separation potential; and breakthrough (PDF)

AUTHOR INFORMATION

Corresponding Authors

Rui-Biao Lin − *MOE Key Laboratory of Bioinorganic and Synthetic Chemistry, School of Chemistry, Sun Yat-Sen University, Guangzhou 510275, P. R. China;* orcid.org/0000-0003-3267-220X; Email: linruibiao@mail.sysu.edu.cn

Banglin Chen − *Department of Chemistry, University of Texas at San Antonio, San Antonio, Texas 78249-0698, United*

States; orcid.org/0000-0001-8707-8115;
Email: banglin.chen@utsa.edu

Authors

Xin Zhang − *Beijing Key Laboratory for Green Catalysis and Separation, Department of Environmental Chemical Engineering, Faculty of Environment and Life, Beijing University of Technology, Beijing 100124, P. R. China; Department of Chemistry, University of Texas at San Antonio, San Antonio, Texas 78249-0698, United States*

Hui Cui − *Department of Chemistry, University of Texas at San Antonio, San Antonio, Texas 78249-0698, United States;* orcid.org/0000-0002-9723-4932

Rajamani Krishna − *Van 't Hoff Institute for Molecular Sciences, University of Amsterdam, 1098 XH Amsterdam, The Netherlands;* orcid.org/0000-0002-4784-8530

Zhi-Yin Zhang − *College of Chemistry and Materials Science, Guangdong Provincial Key Laboratory of Functional Supramolecular Coordination Materials and Applications, Jinan University, Guangzhou 510632, P. R. China*

Ting Liu − *Department of Chemistry, University of Texas at San Antonio, San Antonio, Texas 78249-0698, United States; College of Chemistry and Materials Science, Guangdong Provincial Key Laboratory of Functional Supramolecular Coordination Materials and Applications, Jinan University, Guangzhou 510632, P. R. China*

Bin Liang − *Department of Chemistry, University of Texas at San Antonio, San Antonio, Texas 78249-0698, United States*

Complete contact information is available at: https://pubs.acs.org/10.1021/acsami.1c03923

Notes

The authors declare no competing financial interest.

■ ACKNOWLEDGMENTS

This work was supported by the Grant AX-1730 from the Welch Foundation.

■ REFERENCES

(1) Li, L.; Lin, R.-B.; Krishna, R.; Li, H.; Xiang, S.; Wu, H.; Li, J.; Zhou, W.; Chen, B. Ethane/Ethylene Separation in a Metal−Organic Framework with Iron-Peroxo Sites. *Science* **2018**, *362*, 443−446.

(2) Farrell, B. L.; Igenegbai, V. O.; Linic, S. A Viewpoint on Direct Methane Conversion to Ethane and Ethylene Using Oxidative Coupling on Solid Catalysts. *ACS Catal.* **2016**, *6*, 4340−4346.

(3) Farrell, B. L.; Linic, S. Oxidative Coupling of Methane over Mixed Oxide Catalysts Designed for Solid Oxide Membrane Reactors. *Catal. Sci. Technol.* **2016**, *6*, 4370−4376.

(4) Beck, B.; Fleischer, V.; Arndt, S.; Hevia, M. G.; Urakawa, A.; Hugo, P.; Schomäcker, R. Oxidative Coupling of Methane—a Complex Surface/Gas Phase Mechanism with Strong Impact on the Reaction Engineering. *Catal. Today* **2014**, *228*, 212−218.

(5) Penteado, A. T.; Kim, M.; Godini, H. R.; Esche, E.; Repke, J.-U. Techno-Economic Evaluation of a Biogas-Based Oxidative Coupling of Methane Process for Ethylene Production. *Front. Chem. Sci. Eng.* **2018**, *12*, 598−618.

(6) Kuhl, K. P.; Hatsukade, T.; Cave, E. R.; Abram, D. N.; Kibsgaard, J.; Jaramillo, T. F. Electrocatalytic Conversion of Carbon Dioxide to Methane and Methanol on Transition Metal Surfaces. *J. Am. Chem. Soc.* **2014**, *136*, 14107−14113.

(7) Zandvoort, I.; Ras, E.-J.; Graaf, R.; Krishna, R. Using Transient Breakthrough Experiments for Screening of Adsorbents for Separation of C_2H_4/CO_2 Mixtures. *Sep. Purif. Technol.* **2020**, *241*, No. 116706.

(8) Bachman, J. E.; Reed, D. A.; Kapelewski, M. T.; Chachra, G.; Jonnavittula, D.; Radaelli, G.; Long, J. R. Enabling Alternative Ethylene Production through Its Selective Adsorption in the Metal−Organic Framework Mn_2(M-Dobdc). *Energy Environ. Sci.* **2018**, *11*, 2423−2431.

(9) Jiao, L.; Jiang, H.-L. Metal−Organic-Framework-Based Single-Atom Catalysts for Energy Applications. *Chem* **2019**, *5*, 786−804.

(10) Zhang, T.; Lin, W. Metal−Organic Frameworks for Artificial Photosynthesis and Photocatalysis. *Chem. Soc. Rev.* **2014**, *43*, 5982−5993.

(11) Pang, J.; Di, Z.; Qin, J.-S.; Yuan, S.; Lollar, C. T.; Li, J.; Zhang, P.; Wu, M.; Yuan, D.; Hong, M.; Zhou, H.-C. Precisely Embedding Active Sites into a Mesoporous Zr-Framework through Linker Installation for High-Efficiency Photocatalysis. *J. Am. Chem. Soc.* **2020**, *142*, 15020−15026.

(12) Kim, H.; Yang, S.; Rao, S. R.; Narayanan, S.; Kapustin, E. A.; Furukawa, H.; Umans, A. S.; Yaghi, O. M.; Wang, E. N. Water Harvesting from Air with Metal-Organic Frameworks Powered by Natural Sunlight. *Science* **2017**, *356*, 430−434.

(13) Kalmutzki, M. J.; Diercks, C. S.; Yaghi, O. M. Metal−Organic Frameworks for Water Harvesting from Air. *Adv. Mater.* **2018**, *30*, No. 1704304.

(14) Lu, K.; Aung, T.; Guo, N.; Weichselbaum, R.; Lin, W. Nanoscale Metal−Organic Frameworks for Therapeutic, Imaging, and Sensing Applications. *Adv. Mater.* **2018**, *30*, No. 1707634.

(15) Chen, Y.; Li, P.; Modica, J. A.; Drout, R. J.; Farha, O. K. Acid-Resistant Mesoporous Metal−Organic Framework toward Oral Insulin Delivery: Protein Encapsulation, Protection, and Release. *J. Am. Chem. Soc.* **2018**, *140*, 5678−5681.

(16) Li, H.; Li, L.; Lin, R.-B.; Zhou, W.; Zhang, Z.; Xiang, S.; Chen, B. Porous Metal−Organic Frameworks for Gas Storage and Separation: Status and Challenges. *EnergyChem* **2019**, *1*, No. 100006.

(17) Li, B.; Wen, H.-M.; Zhou, W.; Xu, J. Q.; Chen, B. Porous Metal−Organic Frameworks: Promising Materials for Methane Storage. *Chem* **2016**, *1*, 557−580.

(18) Zhang, X.; Lin, R.-B.; Wang, J.; Wang, B.; Liang, B.; Yildirim, T.; Zhang, J.; Zhou, W.; Chen, B. Optimization of the Pore Structures of MOFs for Record High Hydrogen Volumetric Working Capacity. *Adv. Mater.* **2020**, *32*, No. 1907995.

(19) Chen, Z.; Li, P.; Anderson, R.; Wang, X.; Zhang, X.; Robison, L.; Redfern, L. R.; Moribe, S.; Islamoglu, T.; Gomez-Gualdron, D. A.; Yildirim, T.; Stoddart, J. F.; Farha, O. K. Balancing Volumetric and Gravimetric Uptake in Highly Porous Materials for Clean Energy. *Science* **2020**, *368*, 297−303.

(20) Kundu, T.; Wahiduzzaman, M.; Shah, B. B.; Maurin, G.; Zhao, D. Solvent-Induced Control over Breathing Behavior in Flexible Metal−Organic Frameworks for Natural-Gas Delivery. *Angew. Chem., Int. Ed.* **2019**, *58*, 8073−8077.

(21) Lin, R.-B.; Xiang, S.; Zhou, W.; Chen, B. Microporous Metal−Organic Framework Materials for Gas Separation. *Chem* **2020**, *6*, 337−363.

(22) Niu, Z.; Cui, X.; Pham, T.; Verma, G.; Lan, P. C.; Shan, C.; Xing, H.; Forrest, K. A.; Suepaul, S.; Space, B.; Nafady, A.; Al-Enizi, A. M.; Ma, S. A MOF-based Ultra-Strong Acetylene Nano-trap for Highly Efficient C_2H_2/CO_2 Separation. *Angew. Chem., Int. Ed.* **2021**, *60*, 5283−5288.

(23) Zhao, X.; Wang, Y.; Li, D. S.; Bu, X.; Feng, P. Metal−Organic Frameworks for Separation. *Adv. Mater.* **2018**, *30*, No. 1705189.

(24) Zaworotko, M.; Mukherjee, S.; Kumar, N.; Bezrukov, A. A.; Tan, K.; Pham, T.; Forrest, K. A.; Oyekan, K.; Qazvini, O. T.; Madden, D. G.; Space, B. Amino Functionalised Hybrid Ultra-microporous Materials that Enable Single-Step Ethylene Purification from a Ternary Mixture. *Angew. Chem., Int. Ed.* **2021**, *60*, 10902−10909.

(25) Ye, Y.; Ma, Z.; Lin, R.-B.; Krishna, R.; Zhou, W.; Lin, Q.; Zhang, Z.; Xiang, S.; Chen, B. Pore Space Partition within a Metal−Organic Framework for Highly Efficient C_2H_2/CO_2 Separation. *J. Am. Chem. Soc.* **2019**, *141*, 4130−4136.

(26) Lin, R.-B.; Li, L.; Zhou, H. L.; Wu, H.; He, C.; Li, S.; Krishna, R.; Li, J.; Zhou, W.; Chen, B. Molecular Sieving of Ethylene from

Ethane Using a Rigid Metal−Organic Framework. *Nat. Mater.* **2018**, *17*, 1128−1133.
(27) Cadiau, A.; Adil, K.; Bhatt, P. M.; Belmabkhout, Y.; Eddaoudi, M. A Metal−Organic Framework-Based Splitter for Separating Propylene from Propane. *Science* **2016**, *353*, 137−140.
(28) Liang, B.; Zhang, X.; Xie, Y.; Lin, R.-B.; Krishna, R.; Cui, H.; Li, Z.; Shi, Y.; Wu, H.; Zhou, W.; Chen, B. An Ultramicroporous Metal−Organic Framework for High Sieving Separation of Propylene from Propane. *J. Am. Chem. Soc.* **2020**, *142*, 17795−17801.
(29) Wang, H.; Dong, X.; Colombo, V.; Wang, Q.; Liu, Y.; Liu, W.; Wang, X. L.; Huang, X. Y.; Proserpio, D. M.; Sironi, A.; Han, Y.; Li, J. Tailor-Made Microporous Metal−Organic Frameworks for the Full Separation of Propane from Propylene Through Selective Size Exclusion. *Adv. Mater.* **2018**, *30*, No. 1805088.
(30) Wang, Y.; Jia, X.; Yang, H.; Wang, Y.; Chen, X.; Hong, A. N.; Li, J.; Bu, X.; Feng, P. A Strategy for Constructing Pore-Space-Partitioned MOFs with High Uptake Capacity for C2 Hydrocarbons and CO_2. *Angew. Chem., Int. Ed.* **2020**, *59*, 19027−19030.
(31) Zhai, Q.-G.; Xue, Y.-Y.; Bai, X.-Y.; Zhang, J.; Wang, Y.; Li, S.-N.; Jiang, Y.-C.; Hu, M.-C. Precise Pore Space Partition Combined with High-Density H-Bonding Acceptor within a Metal−Organic Framework for Highly-Efficient Acetylene Storage and Separation. *Angew. Chem., Int. Ed.* **2021**, *60*, 10122−10128.
(32) Bloch, E. D.; Queen, W. L.; Krishna, R.; Zadrozny, J. M.; Brown, C. M.; Long, J. R. Hydrocarbon Separations in a Metal−Organic Framework with Open Iron(II) Coordination Sites. *Science* **2012**, *335*, 1606−1610.
(33) Yoon, J. W.; Chang, H.; Lee, S. J.; Hwang, Y. K.; Hong, D. Y.; Lee, S. K.; Lee, J. S.; Jang, S.; Yoon, T. U.; Kwac, K.; Jung, Y.; Pillai, R. S.; Faucher, F.; Vimont, A.; Daturi, M.; Ferey, G.; Serre, C.; Maurin, G.; Bae, Y. S.; Chang, J. S. Selective Nitrogen Capture by Porous Hybrid Materials Containing Accessible Transition Metal Ion Sites. *Nat. Mater.* **2017**, *16*, 526−531.
(34) Boyd, P. G.; Chidambaram, A.; García-Díez, E.; Ireland, C. P.; Daff, T. D.; Bounds, R.; Gładysiak, A.; Schouwink, P.; Moosavi, S. M.; Maroto-Valer, M. M.; Reimer, J. A.; Navarro, J. A. R.; Woo, T. K.; Garcia, S.; Stylianou, K. C.; Smit, B. Data-Driven Design of Metal−Organic Frameworks for Wet Flue Gas CO_2 Capture. *Nature* **2019**, *576*, 253−256.
(35) Yang, S.; Ramirez-Cuesta, A. J.; Newby, R.; Garcia-Sakai, V.; Manuel, P.; Callear, S. K.; Campbell, S. I.; Tang, C. C.; Schroder, M. Supramolecular Binding and Separation of Hydrocarbons within a Functionalized Porous Metal−Organic Framework. *Nat. Chem.* **2015**, *7*, 121−129.
(36) Zhang, Z.; Peh, S. B.; Wang, Y.; Kang, C.; Fan, W.; Zhao, D. Efficient Trapping of Trace Acetylene from Ethylene in an Ultramicroporous Metal−Organic Framework: Synergistic Effect of High-Density Open Metal and Electronegative Sites. *Angew. Chem., Int. Ed.* **2020**, *59*, 18927−18932.
(37) Zhou, D.-D.; Chen, P.; Wang, C.; Wang, S.-S.; Du, Y.; Yan, H.; Ye, Z.-M.; He, C.-T.; Huang, R.-K.; Mo, Z.-W.; Huang, N.-Y.; Zhang, J.-P. Intermediate-Sized Molecular Sieving of Styrene from Larger and Smaller Analogues. *Nat. Mater.* **2019**, *18*, 994−998.
(38) Lin, R.-B.; Li, L.; Wu, H.; Arman, H.; Li, B.; Lin, R.-G.; Zhou, W.; Chen, B. Optimized Separation of Acetylene from Carbon Dioxide and Ethylene in a Microporous Material. *J. Am. Chem. Soc.* **2017**, *139*, 8022−8028.
(39) Gu, C.; Hosono, N.; Zheng, J.-J.; Sato, Y.; Kusaka, S.; Sakaki, S.; Kitagawa, S. Design and Control of Gas Diffusion Process in a Nanoporous Soft Crystal. *Science* **2019**, *363*, 387−391.
(40) Song, B.-Q.; Yang, Q.-Y.; Wang, S.-Q.; Vandichel, M.; Kumar, A.; Crowley, C.; Kumar, N.; Deng, C.-H.; GasconPerez, V.; Lusi, M.; Wu, H.; Zhou, W.; Zaworotko, M. J. Reversible Switching between Nonporous and Porous Phases of a New SIFSIX Coordination Network Induced by a Flexible Linker Ligand. *J. Am. Chem. Soc.* **2020**, *142*, 6896−6901.
(41) Hiraide, S.; Sakanaka, Y.; Kajiro, H.; Kawaguchi, S.; Miyahara, M. T.; Tanaka, H. High-Throughput Gas Separation by Flexible Metal-Organic Frameworks with Fast Gating and Thermal Management Capabilities. *Nat. Commun.* **2020**, *11*, No. 3867.
(42) Chen, K.-J.; Madden, D. G.; Mukherjee, S.; Pham, T.; Forrest, K. A.; Kumar, A.; Space, B.; Kong, J.; Zhang, Q.-Y.; Zaworotko, M. J. Synergistic Sorbent Separation for One-Step Ethylene Purification from a Four-Component Mixture. *Science* **2019**, *366*, 241−246.
(43) Hao, H.-G.; Zhao, Y.-F.; Chen, D.-M.; Yu, J.-M.; Tan, K.; Ma, S.; Chabal, Y.; Zhang, Z.-M.; Dou, J.-M.; Xiao, Z.-H.; Day, G.; Zhou, H.-C.; Lu, T.-B. Simultaneously Trapping C_2H_2 and C_2H_6 into a Robust Metal−Organic Framework from a Ternary Mixture of C_2H_2/C_2H_4/C_2H_6 for Purification of C_2H_4. *Angew. Chem., Int. Ed.* **2018**, *57*, 16067−16071.
(44) Dong, Q.; Zhang, X.; Liu, S.; Lin, R.-B.; Guo, Y.; Ma, Y.; Yonezu, A.; Krishna, R.; Liu, G.; Duan, J.; Matsuda, R.; Jin, W.; Chen, B. Tuning Gate-Opening of a Flexible Metal−Organic Framework for Ternary Gas Sieving Separation. *Angew. Chem., Int. Ed.* **2020**, *59*, 22756−22762.
(45) Liao, P.-Q.; Zhang, W.-X.; Zhang, J.-P.; Chen, X.-M. Efficient Purification of Ethene by an Ethane-Trapping Metal−Organic Framework. *Nat. Commun.* **2015**, *6*, No. 8697.
(46) Duan, X.; Zhang, Q.; Cai, J.; Yang, Y.; Cui, Y.; He, Y.; Wu, C.; Krishna, R.; Chen, B.; Qian, G. A New Metal−Organic Framework with Potential for Adsorptive Separation of Methane from Carbon Dioxide, Acetylene, Ethylene, and Ethane Established by Simulated Breakthrough Experiments. *J. Mater. Chem. A* **2014**, *2*, 2628−2633.
(47) Li, J.-R.; Kuppler, R. J.; Zhou, H.-C. Selective Gas Adsorption and Separation in Metal−Organic Frameworks. *Chem. Soc. Rev.* **2009**, *38*, 1477−1504.
(48) Queen, W. L.; Hudson, M. R.; Bloch, E. D.; Mason, J. A.; Gonzalez, M. I.; Lee, J. S.; Gygi, D.; Howe, J. D.; Lee, K.; Darwish, T. A.; James, M.; Peterson, V. K.; Teat, S. J.; Smit, B.; Neaton, J. B.; Long, J. R.; Brown, C. M. Comprehensive Study of Carbon Dioxide Adsorption in the Metal−Organic Frameworks M_2(Dobdc) (M = Mg, Mn, Fe, Co, Ni, Cu, Zn). *Chem. Sci.* **2014**, *5*, 4569−4581.
(49) Luo, F.; Yan, C.; Dang, L.; Krishna, R.; Zhou, W.; Wu, H.; Dong, X.; Han, Y.; Hu, T.-L.; O'Keeffe, M.; Wang, L.; Luo, M.; Lin, R. B.; Chen, B. UTSA-74: A MOF-74 Isomer with Two Accessible Binding Sites per Metal Center for Highly Selective Gas Separation. *J. Am. Chem. Soc.* **2016**, *138*, 5678−5684.
(50) Caskey, S. R.; Wong-Foy, A. G.; Matzger, A. J. Dramatic Tuning of Carbon Dioxide Uptake via Metal Substitution in a Coordination Polymer with Cylindrical Pores. *J. Am. Chem. Soc.* **2008**, *130*, 10870−10871.
(51) Chen, C. X.; Wei, Z. W.; Pham, T.; Lan, P. C.; Zhang, L.; Forrest, K. A.; Chen, S.; Al-Enizi, A. M.; Nafady, A.; Su, C. Y.; Ma, S. Nanospace Engineering of Metal−Organic Frameworks through Dynamic Spacer Installation of Multifunctionalities for Efficient Separation of Ethane from Ethane/Ethylene Mixtures. *Angew. Chem., Int. Ed.* **2021**, *60*, 9680−9685.
(52) Rosi, N. L.; Kim, J.; Eddaoudi, M.; Chen, B.; O'Keeffe, M.; Yaghi, O. M. Rod Packings and Metal−Organic Frameworks Constructed from Rod-Shaped Secondary Building Units. *J. Am. Chem. Soc.* **2005**, *127*, 1504−1518.
(53) Chui, S. S.-Y.; Lo, S. M.-F.; Charmant, J. P.; Orpen, A. G.; Williams, I. D. A Chemically Functionalizable Nanoporous Material $[Cu_3(TMA)_2(H_2O)]_3]_n$. *Science* **1999**, *283*, 1148−1150.
(54) Xiang, S.; Zhou, W.; Gallegos, J. M.; Liu, Y.; Chen, B. Exceptionally High Acetylene Uptake in a Microporous Metal−Organic Framework with Open Metal Sites. *J. Am. Chem. Soc.* **2009**, *131*, 12415−12419.
(55) Myers, A. L.; Prausnitz, J. M. Thermodynamics of Mixed-Gas Adsorption. *AlChE J.* **1965**, *11*, 121−127.
(56) Krishna, R. Screening Metal−Organic Frameworks for Mixture Separations in Fixed-Bed Adsorbers Using a Combined Selectivity/Capacity Metric. *RSC Adv.* **2017**, *7*, 35724−35737.

https://doi.org/10.1021/acsami.1c03923
ACS Appl. Mater. Interfaces 2021, 13, 22514−22520

Supporting Information

Realization of ethylene production from its quaternary mixture through metal-organic framework materials

Xin Zhang,[a,b] Hui Cui,[b] Rui-Biao Lin,[b,c] Rajamani Krishna,[d] Zhi-Yin Zhang,[e] Ting Liu,[b,e] Bin Liang,[b] and Banglin Chen[b]**

[a]Beijing Key Laboratory for Green Catalysis and Separation, Department of Environmental Chemical Engineering, Faculty of Environment and Life, Beijing University of Technology, Beijing 100124, P. R. China

[b]Department of Chemistry, University of Texas at San Antonio, One UTSA Circle, San Antonio, Texas 78249-0698, United States.

[c]MOE Key Laboratory of Bioinorganic and Synthetic Chemistry, School of Chemistry, Sun Yat-Sen University, Guangzhou, 510275, China

[d] Van 't Hoff Institute for Molecular Sciences, University of Amsterdam, 1098 XH Amsterdam, The Netherlands

[e]College of Chemistry and Materials Science, Guangdong Provincial Key Laboratory of Functional Supramolecular Coordination Materials and Applications, Jinan University, Guangzhou 510632, P. R. China.

1. Powder X-ray diffraction

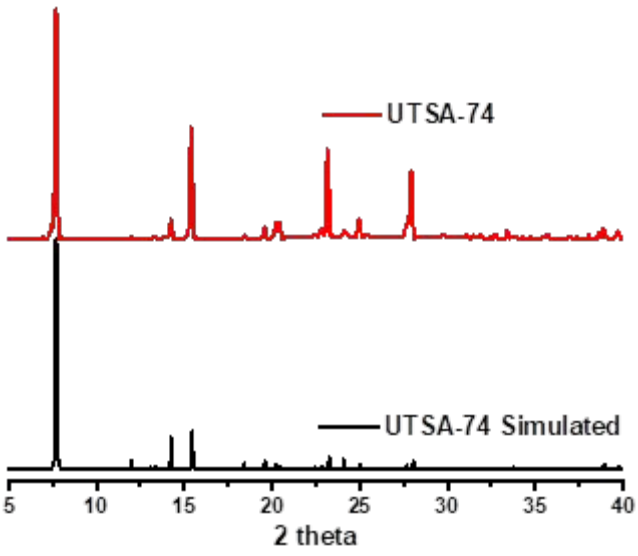

Figure S1. PXRD of UTSA-74.

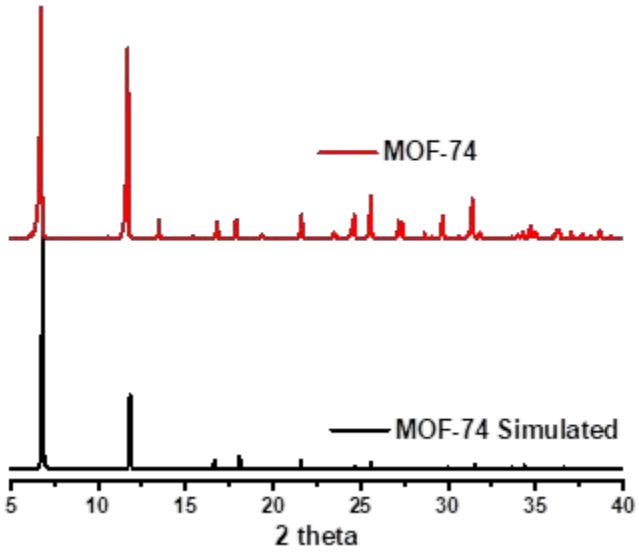

Figure S2. PXRD of MOF-74.

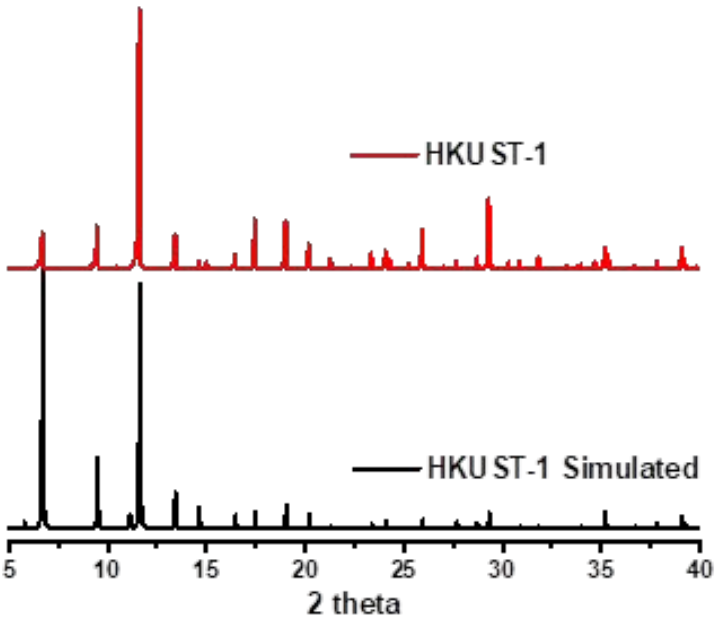

Figure S3. PXRD of HKUST-1.

2. Adsorption isotherms

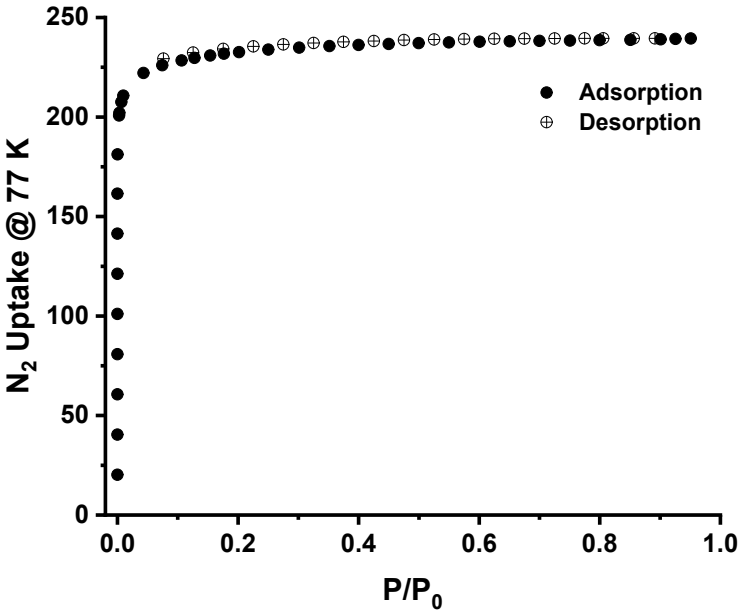

Figure S4. N_2 adsorption isotherm of UTSA-74 at 77 K.

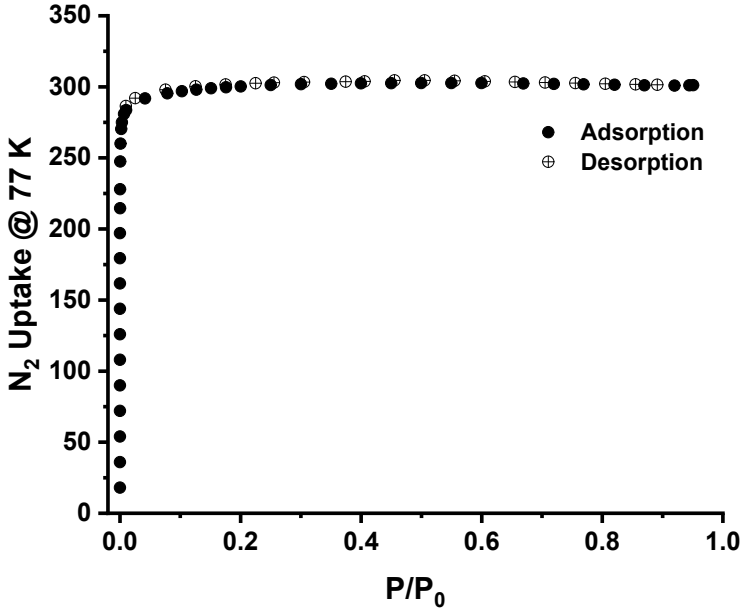

Figure S5. N_2 adsorption isotherm of MOF-74 at 77 K.

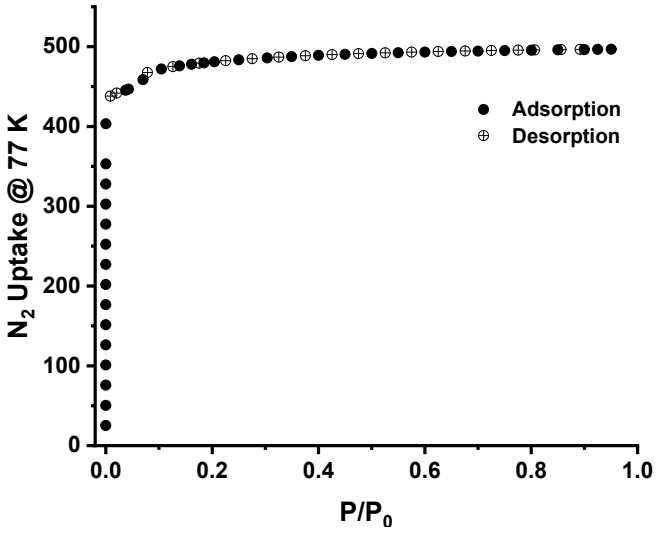

Figure S6. N_2 adsorption isotherm of HKUST-1 at 77 K.

Table S1. Comparison of adsorption properties.

MOF	V_p	Theoretical V_p	Crystal density	OMS density	C_2H_4 adsorption	C_2H_4 to OMS ratio	C_2H_4 packing density
MOF-74	0.47 cm^3/g	0.46 cm^3/g	1.219 g/cm^3	6.2 mmol/g	5.9 mmol/g	0.95	12.6 $mmol/cm^3$
UTSA-74	0.37 cm^3/g	0.36 cm^3/g	1.34 g/cm^3	6.2 mmol/g	4.6 mmol/g	0.74	12.4 $mmol/cm^3$
HKUST-1	0.77 cm^3/g	0.75 cm^3/g	0.879 g/cm^3	2.5 mmol/g	7.8 mmol/g	3.12	10.1 $mmol/cm^3$

Note: theoretical Vp was calculated by PLATON using probe of 1.8 Å; C_2H_4 adsorption based on isotherms measured at 298 K.

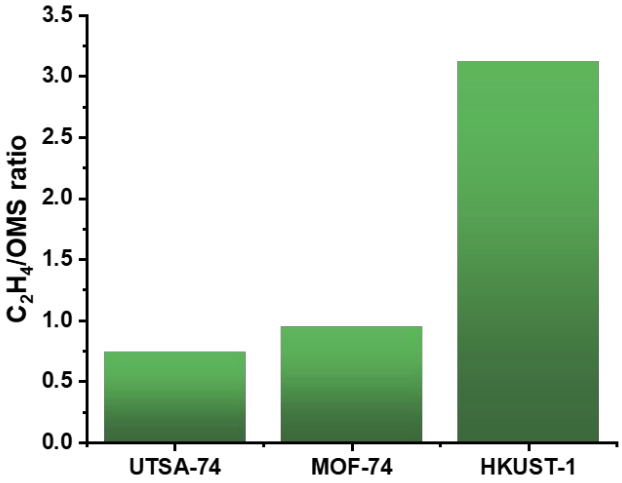

Figure S7. Molar ratio of adsorbed C_2H_4 to open metal sites.

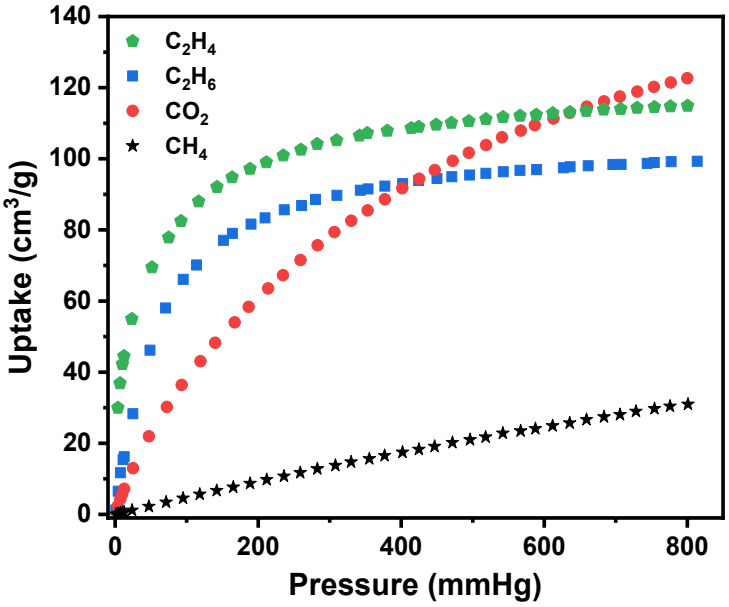

Figure S8. Adsorption isotherms of UTSA-74 at 273 K.

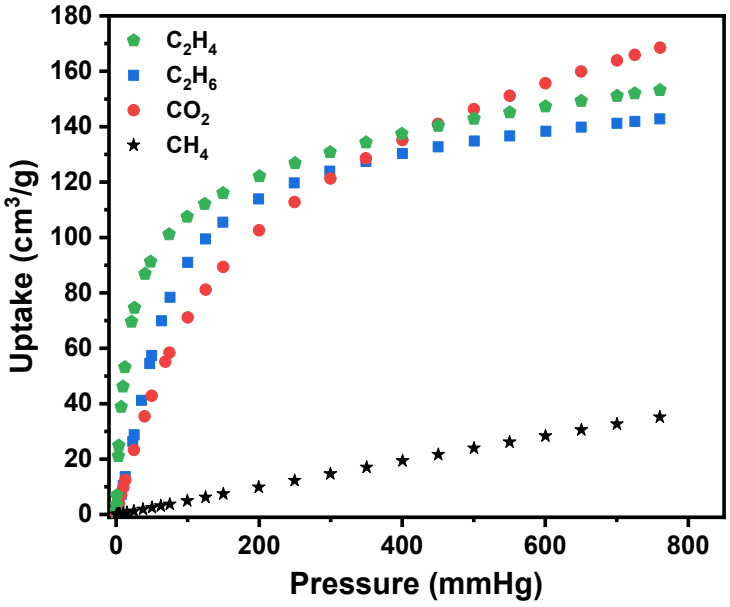

Figure S9. Adsorption isotherms of MOF-74 at 273 K.

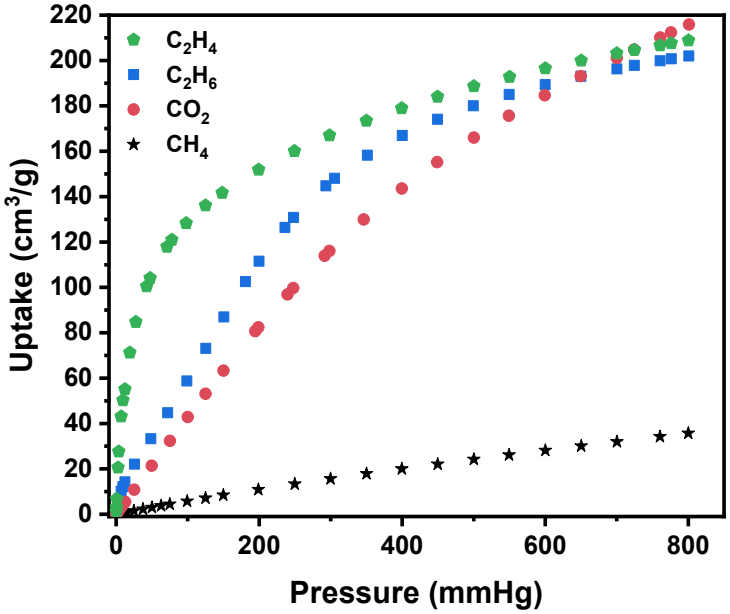

Figure S10. Adsorption isotherms of HKUST-1 at 273 K.

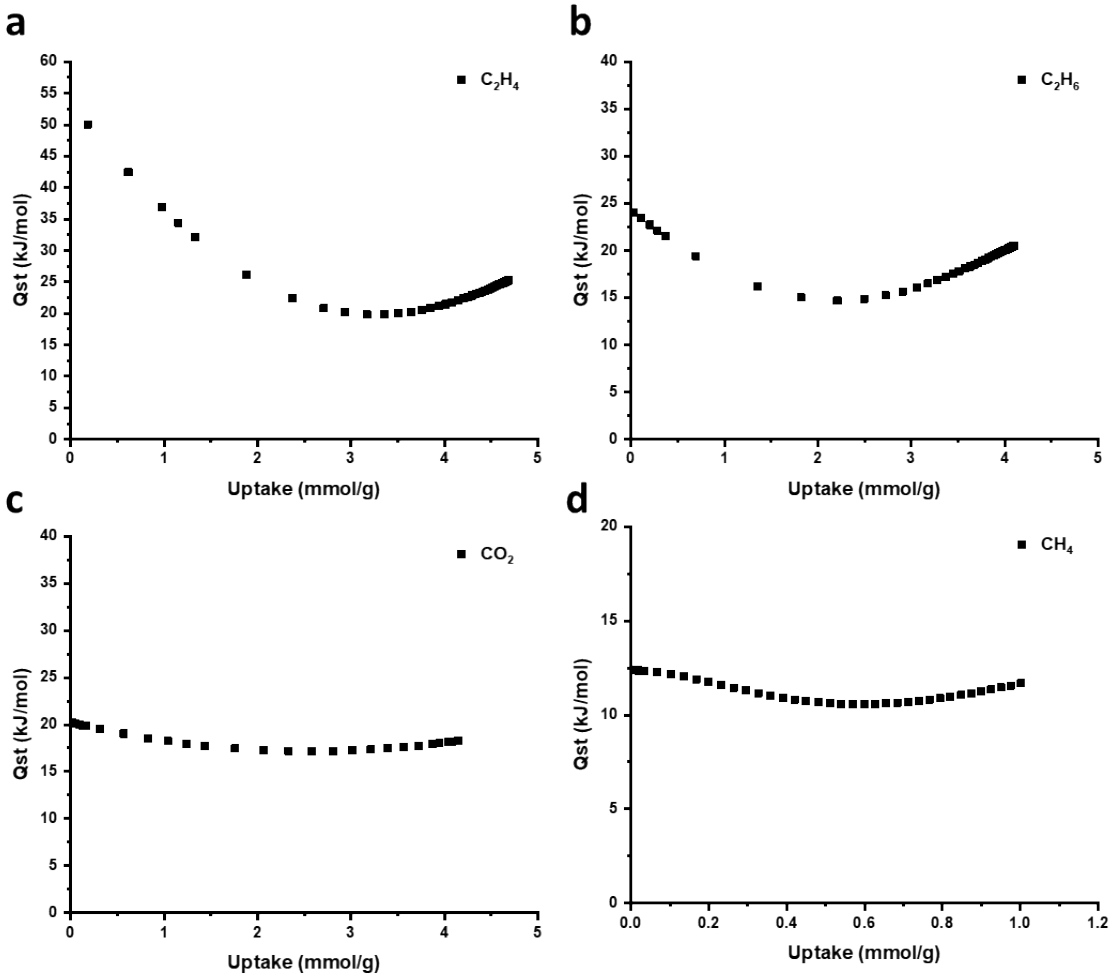

Figure S11. Qst of UTSA-74 for C_2H_4, C_2H_6, CO_2, and CH_4 determined using Virial method with isotherms at 298 K and 273 K.

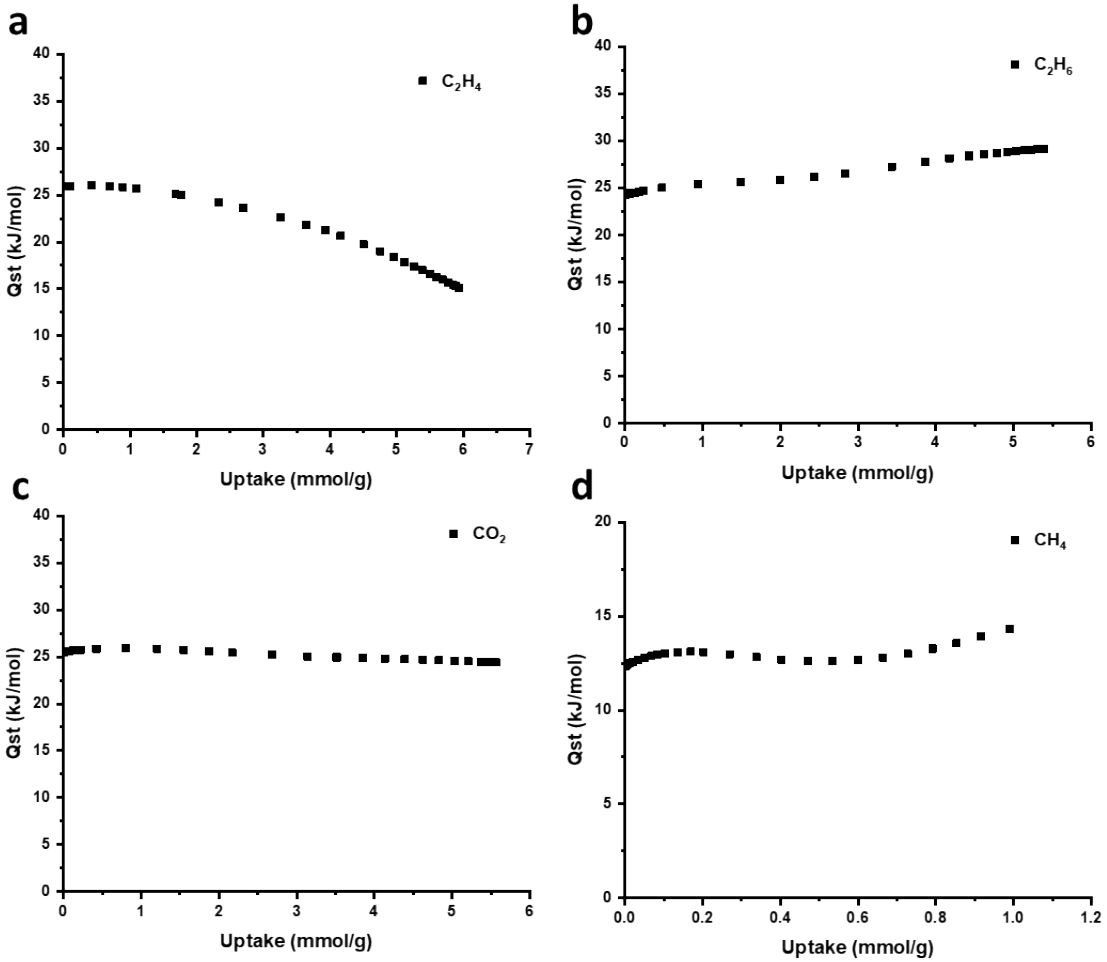

Figure S12. Qst of MOF-74 for C_2H_4, C_2H_6, CO_2, and CH_4 determined using Virial method with isotherms at 298 K and 273 K.

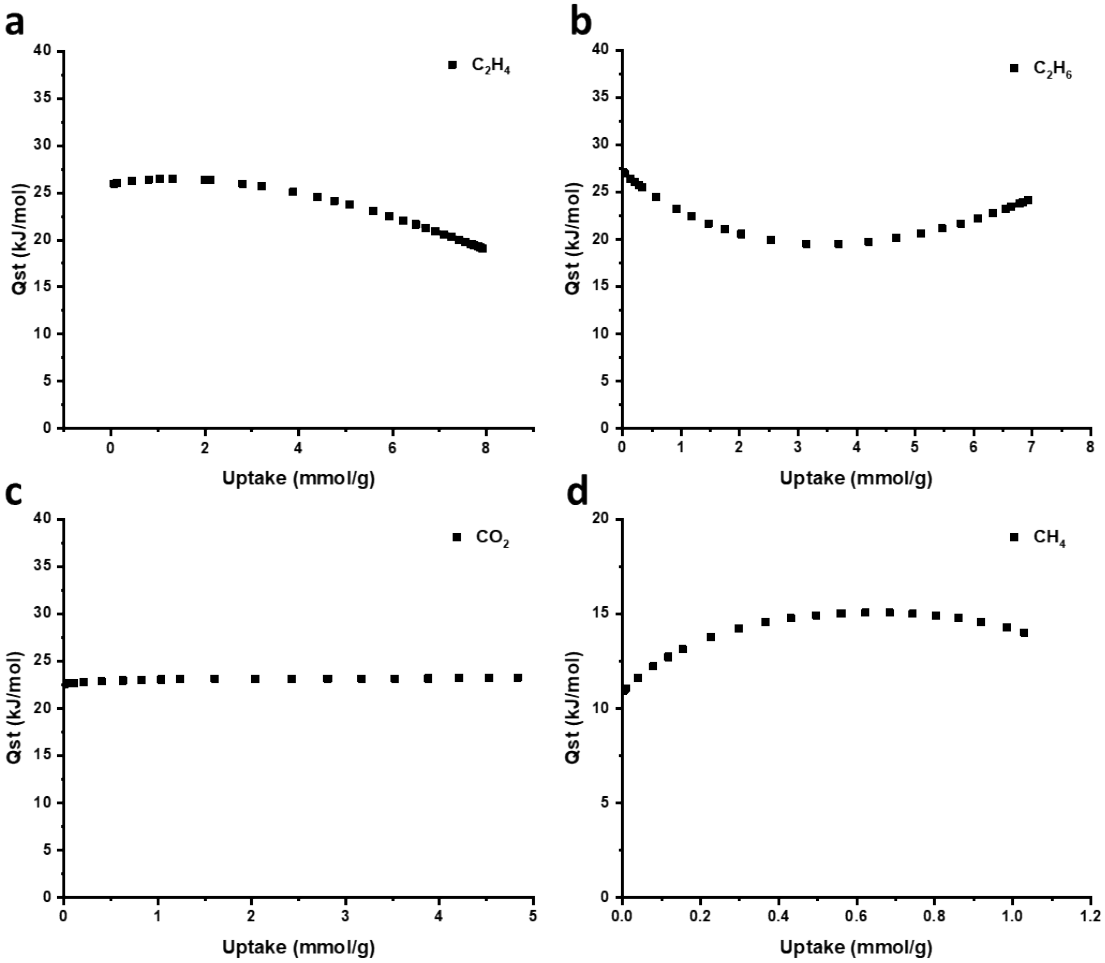

Figure S13. Qst of HKUST-1 for C_2H_4, C_2H_6, CO_2, and CH_4 determined using Virial method with isotherms at 298 K and 273 K. The increased Qst of C_2H_6 at high loading indicates that the guest-guest interaction increases likely due to pore filling effect.[1]

3. Calculation of IAST selectivity and separation potential

The unary isotherms for C_2H_4 at 298 K in UTSA-74, ZnMOF-74, and HKUST-1 were fitted with excellent accuracy using either the dual-site Langmuir model, where we distinguish two distinct adsorption sites A and B:

$$q = \frac{q_{sat,A} b_A p}{1 + b_A p} + \frac{q_{sat,B} b_B p}{1 + b_B p} \quad \text{(S1)}$$

The unary isotherms for C_2H_6 at 298 K in UTSA-74, ZnMOF-74, and HKUST-1 were fitted with the 1-site Langmuir-Freundlich isotherm with excellent accuracy

$$q = \frac{q_{sat,A} b_A p^{\nu}}{1 + b_A p^{\nu}} \quad \text{(S2)}$$

The unary isotherms for CO_2, and CH_4 at 298 K in UTSA-74, ZnMOF-74, and HKUST-1 wee fitted with the 1-site Langmuir isotherm with excellent accuracy

$$q = \frac{q_{sat,A} b_A p}{1 + b_A p} \quad \text{(S3)}$$

The unary isotherm fit parameters for each of the 3 MOFs are provided in Table S, Table S, and Table S4.

The unary isotherm data for Mn_2(*m*-dobdc), ZJNU-49, NOTT-300, and HOF-3 were taken from the original literature sources.

Table S2. Parameter fits for C_2H_4, C_2H_6, CO_2, and CH_4 in HKUST-1.

	Site A			Site B		
	$q_{A,sat}$ mol kg^{-1}	b_A Pa$^{-\nu_A}$	ν_A	$q_{B,sat}$ mol kg^{-1}	b_B Pa$^{-\nu_B}$	ν_A
C_2H_4	6	5.705E-06	1	6	1.534E-04	1
C_2H_6	14.5	8.890E-06	1			
CO_2	22	3.230E-06	1			
CH_4	6	1.957E-06	1			

Table S3. Parameter fits for C_2H_4, C_2H_6, CO_2, and CH_4 in UTSA-74.

	Site A			Site B		
	$q_{A,sat}$ mol kg^{-1}	b_A Pa$^{-\nu_A}$	ν_A	$q_{B,sat}$ mol kg^{-1}	b_B Pa$^{-\nu_B}$	ν_A
C_2H_4	3.6	5.812E-05	1	1.6	9.690E-04	1
C_2H_6	4.5	1.815E-05	1.15			
CO_2	7.2	1.248E-05	1			
CH_4	8	1.365E-06	1			

Table S4. Parameter fits for C_2H_4, C_2H_6, CO_2, and CH_4 in ZnMOF-74.

	Site A			Site B		
	$q_{A,sat}$ mol kg^{-1}	b_A Pa$^{-\nu_A}$	ν_A	$q_{B,sat}$ mol kg^{-1}	b_B Pa$^{-\nu_B}$	ν_A
C_2H_4	3.7	4.030E-06	1	5.2	1.500E-04	1
C_2H_6	6.4	5.446E-06	1.2			
CO_2	9.1	1.574E-05	1			
CH_4	15	6.983E-07	1			

For $C_2H_4(1)/C_2H_6(2)/CO_2(3)/CH_4(4)$ mixture separations, three adsorption selectivities for $C_2H_4(1)/C_2H_6(2)$, $C_2H_4(1)/CO_2(3)$, and $C_2H_4(1)/CH_4(4)$ pairs may be defined

$$S_{ads12} = \frac{q_1/q_2}{y_{10}/y_{20}}; S_{ads13} = \frac{q_1/q_3}{y_{10}/y_{30}}; S_{ads14} = \frac{q_1/q_4}{y_{10}/y_{40}}; \quad \text{(S4)}$$

In eq (S4), $y_{10}, y_{20}, y_{30}, y_{40} = 0.25$ are the mole fractions of the bulk gas phase mixture. The molar loadings q_1, q_2, q_3, q_4 of the four components are determined using the Ideal Adsorbed Solution Theory (IAST) of Myers and Prausnitz using the unary isotherm fits as data inputs.[2] **Error! Reference source not found.** presents IAST calculations of the adsorption selectivities for 25/25/25/25 $C_2H_4/C_2H_6/CO_2/CH_4$ mixtures at 298 K as function of the total bulk gas phase pressure, p_t, in UTSA-74, ZnMOF-74, and HKUST-1. At p_t = 100 kPa, it is noted that HKUST-1 has the highest selectivities for the three binary pairs.

The $C_2H_4(1)/C_2H_6(2)/CO_2(3)/CH_4(4)$ mixture separations are envisaged to be carried out in fixed bed adsorbers. In such devices, the separations are dictated by a combination of adsorption selectivity and uptake capacity. For all three MOFs, UTSA-74, ZnMOF-74, and HKUST-1, the desired product $C_2H_4(1)$ can be recovered as pure

component only in the desorption phase. Using the shock wave model for fixed bed adsorbers, Krishna[3-4] has suggested that the appropriate metric is the separation potential, Δq. The appropriate expression describing the productivity of pure C_2H_4 in the desorption phase of fixed-bed operations is

$$\Delta q = q_1 - \left(q_2 + q_3 + q_4\right)\frac{y_{10}}{y_{20} + y_{30} + y_{40}} \quad \text{(S5)}$$

In eq (S5), $y_{10}, y_{20}, y_{30}, y_{40} = 0.25$ are the mole fractions of the feed mixture during the adsorption cycle. In the derivation of eq (S5), it is assumed that the concentration "fronts" traversed the column in the form of shock waves during the desorption cycle. The molar loadings q_1, q_2, q_3, q_4 of the four components are determined using the Ideal Adsorbed Solution Theory (IAST) of Myers and Prausnitz using the unary isotherm fits as data inputs.[2] The physical significance of Δq is the maximum productivity of pure C_2H_4(1) that is achievable in fixed bed adsorbers; it may be considered as a combined selectivity-capacity matrix.

Figure 4b and Table S5 presents IAST calculations of the Δq and the C_2H_4 uptake, in 25/25/25/25 $C_2H_4/C_2H_6/CO_2/CH_4$ mixtures at 298 K and 100 kPa. It is noteworthy that

HKUST-1 has the highest Δq value and we should therefore expect HKUST-1 to have the highest productivity of pure C_2H_4 in the desorption phase of PSA operations.

4. Transient breakthrough simulations

We describe below the simulation methodology used to perform transient breakthrough calculations for fixed bed adsorbers (see schematic in 14). The simulation methodology is the same as used in our earlier publications.[3-7] For an *n*-component gas mixture flowing through a fixed bed maintained under isothermal, isobaric, conditions, the molar concentrations in the gas phase at any position and instant of time are obtained by solving the following set of partial differential equations for each of the species *i* in the gas mixture[6, 8-10]

$$-D_{ax}\frac{\partial^2 c_i(t,z)}{\partial z^2}+\frac{\partial c_i(t,z)}{\partial t}+\frac{\partial\left(v(t,z)c_i(t,z)\right)}{\partial z}+\frac{\left(1-\varepsilon\right)}{\varepsilon}\rho\frac{\partial \bar{q}_i(t,z)}{\partial t}=0;\quad i=1,2,...n \tag{S6}$$

In eq (S6), t is the time, z is the distance along the adsorber, ρ is the framework density, ε is the bed voidage, D_{ax} is the axial dispersion coefficient, v is the interstitial gas velocity, and $\bar{q}_i(t,z)$ is the *spatially averaged* molar loading within the crystallites of radius r_c, monitored at position z, and at time t. The time $t = 0$, corresponds to the time at which the feed mixture is injected at the inlet to the fixed bed. Prior to injection of the feed

mixture, N_2 gas flows through the fixed bed. In this model described by eq (S6), the effects of all mechanisms that contribute to axial mixing are lumped into a single effect axial dispersion coefficient D_{ax}. Axial dispersion effects are ignored in the breakthrough simulations reported in this work.

The radial distribution of molar loadings, q_i, within a spherical crystallite, of radius r_c, is obtained from a solution of a set of differential equations describing the uptake

$$\rho \frac{\partial q_i(r,t)}{\partial t} = -\frac{1}{r^2}\frac{\partial}{\partial r}\left(r^2 N_i\right) \tag{S7}$$

The intra-crystalline fluxes N_i, in turn, are related to the radial gradients in the molar loadings by the Maxwell-Stefan (M-S) diffusion equations

$$N_i = -\rho Đ_i \frac{\partial q_i}{\partial r}; \quad i = 1,2..n \tag{S8}$$

For all times $t \geq 0$, the exterior of the crystal is brought into contact with a bulk gas mixture at partial pressures p_{i0} that is maintained constant till the crystal reaches thermodynamic equilibrium with the surrounding gas mixture. At any time t, the component loadings at the surface of the particle $q_i(r_c,t) = q_i^*$ is in equilibrium with the bulk phase gas mixture with partial pressures p_{i0}. In the general case, the component

loadings are calculated using the Ideal Adsorbed Solution Theory (IAST) of Myers and Prausnitz.[2]

At any time *t*, during the transient approach to thermodynamic equilibrium, the spatial-averaged component loading within the crystallites of radius r_c is calculated using

$$\bar{q}_i(t) = \frac{3}{r_c^3}\int_0^{r_c} q_i(r,t) r^2 dr \tag{S9}$$

Summing equation (S9) over all *n* species in the mixture allows calculation of the *total average* molar loading of the mixture within the crystallite

$$\bar{q}_t(t,z) = \sum_{i=1}^{n} \bar{q}_i(t,z) \tag{S10}$$

The term $\frac{\partial \bar{q}_i(t,z)}{\partial t}$ in equation (S6) is determined by solving the set of equations (S7), and (S9), and (S10). At any time *t*, and position *z*, the component loadings at the outer surface of the particle $q_i(r_c,t,z)$ is in equilibrium with the bulk phase gas mixture with partial pressures $p_i(t,z)$ in the bulk gas mixture. In the general case, the component loadings $q_i(r_c,t,z)$ are calculated using the Ideal Adsorbed Solution Theory (IAST) of Myers and Prausnitz.[2]

In all of the simulations presented in this article the value of $\frac{Đ_i}{r_c^2}$ is assumed to be large enough to ensure that intra-crystalline gradients are absent and the entire crystallite particle can be considered to be in thermodynamic equilibrium with the surrounding bulk gas phase at that time *t*, and position *z* of the adsorber

$$\bar{q}_i(t,z) = q_i(t,z) \tag{S11}$$

The *interstitial* gas velocity is related to the *superficial* gas velocity by

$$v = \frac{u}{\varepsilon} \tag{S12}$$

At time, t = 0, the inlet to the adsorber, z = 0, is subjected to a step input of the *n*-component gas mixture and this step input is maintained till the end of the adsorption cycle when steady-state conditions are reached.

$$t \geq 0; \quad p_i(0,t) = p_{i0}; \quad u(0,t) = u_0 \tag{S13}$$

where $u_0 = v_0\varepsilon$ is the superficial gas velocity at the inlet to the adsorber.

For simulations of the desorption cycle, we use a purge gas that is non-adsorbing (e.g. helium) that is fed to the fixed bed at the same superficial gas velocity $u_0 = v_0\varepsilon$ as in the adsorption cycle. The total pressure of the adsorbing components (1, 2, ..*n*) is

maintained at 0.2 Pa. This choice ensures that the desorption cycle is operated under deep vacuum.

For comparing the separation performance of MOFs, we carried out simulations of transient desorption in which we choose: cross-sectional area, A = 1 m^2; superficial gas velocity at the entrance to the bed, u_0 = 0.04 m s^{-1}; voidage of the packed bed, ε = 0.4. We choose the mass of the adsorbent in the bed $m_{ads} = 180$ kg, cross-sectional area, A = 1 m^2; superficial gas velocity at the bed inlet, u_0 = 0.04 m s^{-1}; voidage of the packed bed, ε = 0.4. If the total length of the bed is L m, the total volume of the bed is $V_{bed} = LA$. The volume of MOF crystals used in the simulations is $V_{ads} = LA(1-\varepsilon)$. It is important to note that the volume of adsorbent, V_{ads}, includes the pore volume of the adsorbent material. If ρ is the framework density, the mass of the adsorbent in the bed is $m_{ads} = (1-\varepsilon)\times(L \text{ m})\times(A \text{ m}^2)\times(\rho \text{ kg m}^{-3})$ kg. The length L of the adsorber bed is chosen as $L = \dfrac{180}{(1-\varepsilon)\rho} = \dfrac{300}{\rho}$ m.

The crystal framework densities are

UTSA-74: $\rho = 1340 \text{ kg m}^{-3}$; ZnMOF-74: $\rho = 1231 \text{ kg m}^{-3}$; HKUST-1: $\rho = 879 \text{ kg m}^{-3}$.

Therefore, the packed bed lengths are chosen as follows: UTSA-74: $L = 0.223881$ m; ZnMOF-74: $L = 0.243704$ m; HKUST-1: $L = 0.341297$ m.

With the above choice of lengths of the packed beds, the mass of adsorbent in the bed is precisely $m_{ads} = 180$ kg for all three MOFs.

In all the simulations reported here, the total pressure is assumed to be constant along the length of the fixed bed. All the reported transient breakthrough simulations are performed at 298 K and $p_t = 10^5$ Pa total pressure.

For presenting the breakthrough simulation results, we use the dimensionless time, $\tau = \frac{tu}{L\varepsilon}$, obtained by dividing the actual time, *t*, by the characteristic time, $\frac{L}{v} = \frac{\varepsilon L}{u_0}$, where *L* is the length of adsorber, *v* is the interstitial gas velocity.

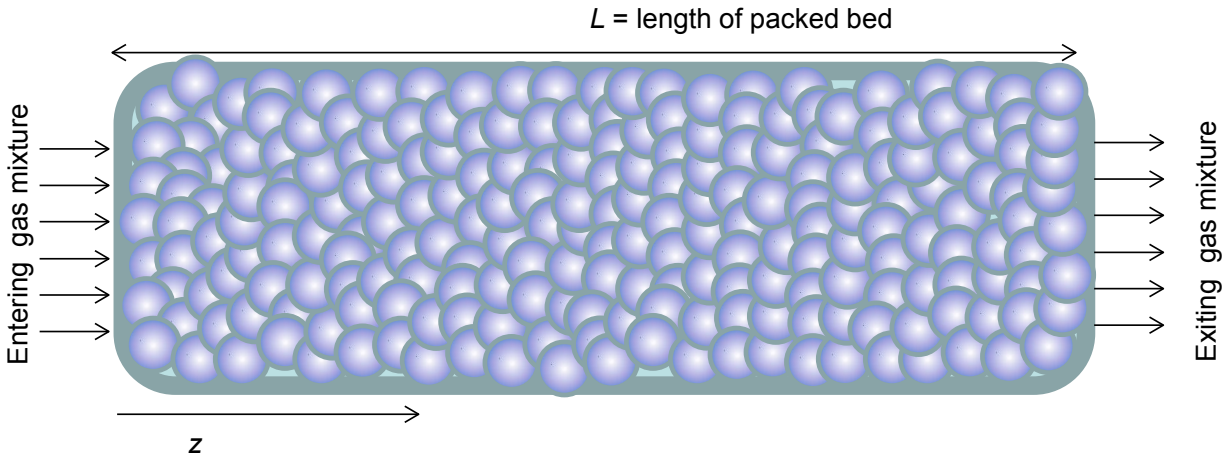

Figure S14. Schematic of fixed bed adsorber.

Figure Sa presents the transient breakthrough simulations for the adsorption phase of 25/25/25/25 $C_2H_4/C_2H_6/CO_2/CH_4$ mixture in a fixed bed adsorber packed with HKUST-1, operating at 100 kPa and 298 K. The desired C_2H_4 product can only be recovered in the desorption, i.e. blowdown, cycle of PSA operations. 15b presents simulations of the corresponding desorption cycle in which the equilibrated bed is subject to deep vacuum (4 Pa). During the time interval indicated by the arrow, C_2H_4 of the desired purity can be recovered. The amount of 99%+ pure C_2H_4 can be determined from a material balance on the adsorber in the desorption cycle. Analogous breakthrough simulations such as presented in Figure S15 for HKUST-1 were performed also for MOF-74 (Figure S16) and UTSA-74 (Figure S17).

These productivity values, expressed as mole of desired C_2H_4 product (of 99%+ purity) per kg of adsorbent in packed bed for the three different MOFs are plotted in **Error! Reference source not found.**4b and S19. The *x*-axis in **Error! Reference source not found.** is the separation potential, Δq, that is determined from IAST calculations using eq (S5).

Table S5. Calculation results for mixture breakthrough separation.

C_2H_4 Uptake in mixture	Separation potential	Productivity of 99%+
2.77 mmol/g	2.30 mmol/g	1.25 mmol/g
3.22 mmol/g	2.50 mmol/g	1.52 mmol/g
4.72 mmol/g	4.09 mmol/g	2.97 mmol/g

We note that the productivities determined from the transient breakthrough simulations (denoted as symbols) are linearly related to Δq. The actual productivities are lower than the Δq values because of the distended nature of the transient desorption breakthroughs. It is noteworthy that HKUST-1 has the highest productivity value, in line with the expectations of the Δq values.

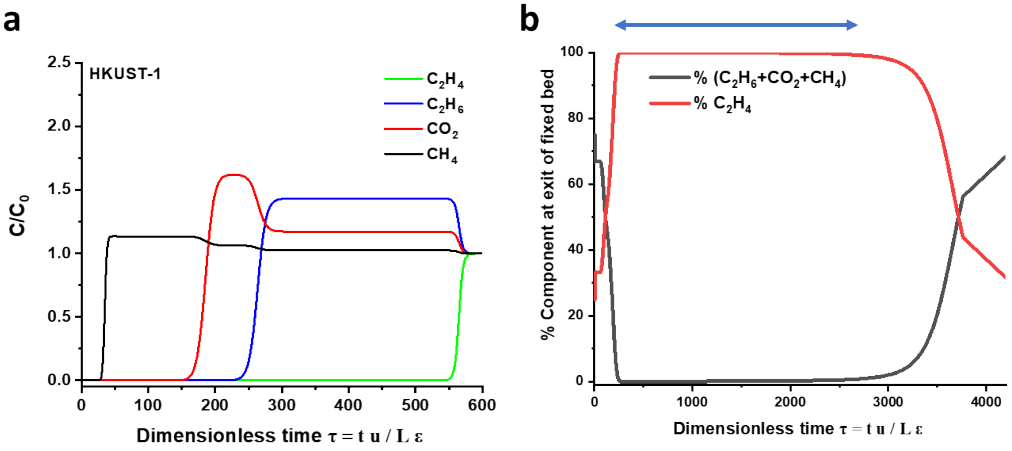

Figure S15. (a) Simulations of transient breakthroughs of 25/25/25/25 $C_2H_4/C_2H_6/CO_2/CH_4$ mixtures in fixed bed packed with HKUST-1 operating at 298 K and 100 kPa . (b) Simulations of transient desorption (blowdown) under deep vacuum (4 Pa total pressure) and 298 K. During the time interval indicated by the arrow, C_2H_4 product containing < 1% (C_2H_6+CO_2+CH_4) can be recovered.

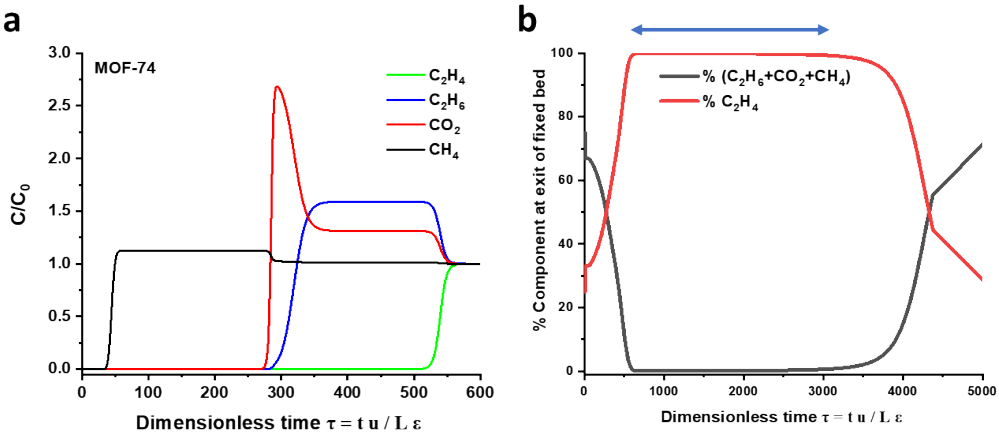

Figure S16. (a) Simulations of transient breakthroughs of 25/25/25/25 $C_2H_4/C_2H_6/CO_2/CH_4$ mixtures in fixed bed packed with MOF-74 operating at 298 K and 100 kPa . (b) Simulations of transient desorption (blowdown) under deep vacuum (4 Pa total pressure) and 298 K. During the time interval indicated by the arrow, C_2H_4 product containing < 1% (C_2H_6+CO_2+CH_4) can be recovered.

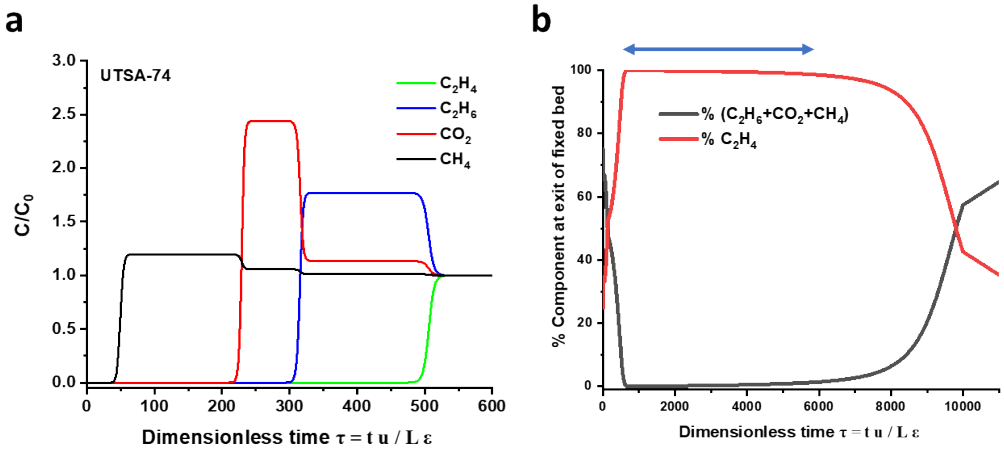

Figure S17. (a) Simulations of transient breakthroughs of 25/25/25/25 $C_2H_4/C_2H_6/CO_2/CH_4$ mixtures in fixed bed packed with UTSA-74 operating at 298 K and 100 kPa . (b) Simulations of transient desorption (blowdown) under deep vacuum (4 Pa total pressure) and 298 K. During the time interval indicated by the arrow, C_2H_4 product containing < 1% (C_2H_6+CO_2+CH_4) can be recovered.

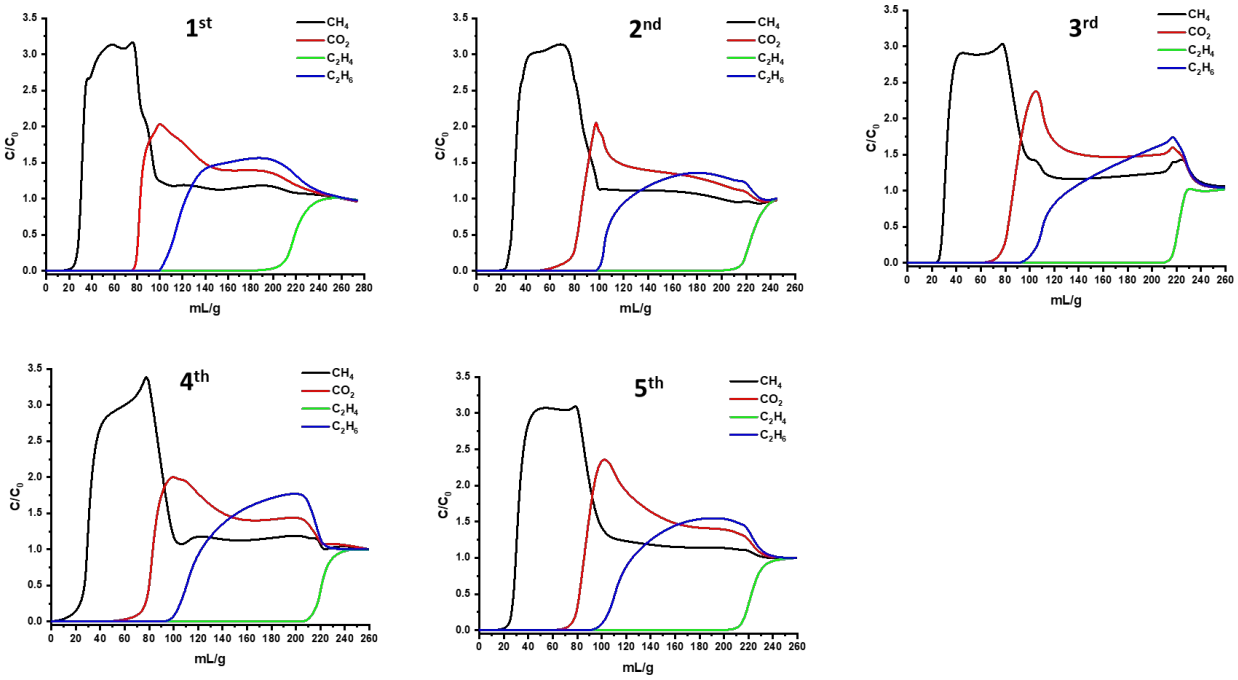

Figure S18. Five experimental breakthrough cycles of HKUST-1.

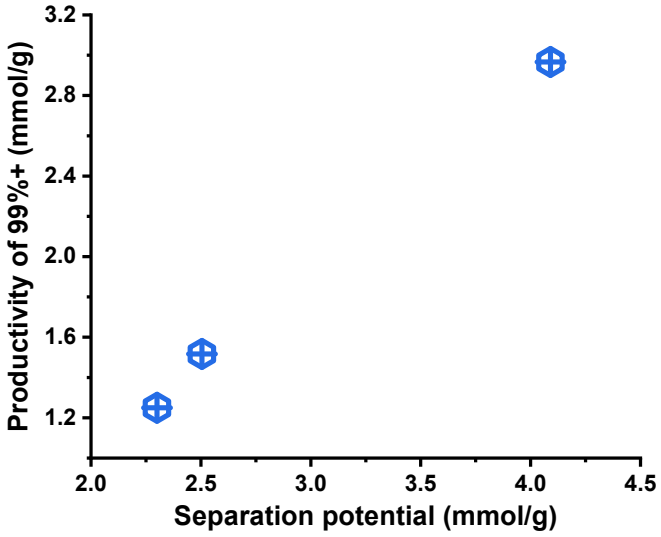

Figure S19. Comparison of separation potential and productivity for UTSA-74, MOF-74 and HKUST-1.

References

(1) Queen, W. L.; Hudson, M. R.; Bloch, E. D.; Mason, J. A.; Gonzalez, M. I.; Lee, J. S.; Gygi, D.; Howe, J. D.; Lee, K.; Darwish, T. A.; James, M.; Peterson, V. K.; Teat, S. J.; Smit, B.; Neaton, J. B.; Long, J. R.; Brown, C. M. Comprehensive study of carbon dioxide adsorption in the metal–organic frameworks M2(dobdc) (M = Mg, Mn, Fe, Co, Ni, Cu, Zn). *Chem. Sci.* **2014,** *5* (12), 4569-4581.
(2) Myers, A. L.; Prausnitz, J. M. Thermodynamics of Mixed Gas Adsorption. *A.I.Ch.E.J.* **1965,** *11*, 121-130.
(3) Krishna, R. Screening Metal-Organic Frameworks for Mixture Separations in Fixed-Bed Adsorbers using a Combined Selectivity/Capacity Metric. *RSC Advances* **2017,** *7*, 35724-35737.
(4) Krishna, R. Metrics for Evaluation and Screening of Metal-Organic Frameworks for Applications in Mixture Separations. *ACS Omega* **2020,** *5*, XXX-XXX.
(5) Krishna, R. Methodologies for Evaluation of Metal-Organic Frameworks in Separation Applications. *RSC Advances* **2015,** *5*, 52269-52295.
(6) Krishna, R. The Maxwell-Stefan Description of Mixture Diffusion in Nanoporous Crystalline Materials. *Microporous Mesoporous Mater.* **2014,** *185*, 30-50.
(7) Krishna, R. Tracing the Origins of Transient Overshoots for Binary Mixture Diffusion in Microporous Crystalline Materials. *Phys. Chem. Chem. Phys.* **2016,** *18*, 15482-15495.
(8) Krishna, R.; Baur, R. Modelling Issues in Zeolite Based Separation Processes. *Sep. Purif. Technol.* **2003,** *33*, 213-254.
(9) Krishna, R.; Baur, R. Diffusion, Adsorption and Reaction in Zeolites: Modelling and Numerical Issues. http://krishna.amsterchem.com/zeolite/ (accessed 17 April 2020).
(10) Ruthven, D. M.; Farooq, S.; Knaebel, K. S. *Pressure swing adsorption*, VCH Publishers: New York, 1994.